IEEE Access
Multidisciplinary | Rapid Review | Open Access Journal

Received December 9, 2019, accepted December 22, 2019, date of publication December 26, 2019, date of current version January 6, 2020.

Digital Object Identifier 10.1109/ACCESS.2019.2962570

Study on the Reading of Energy-Harvested Implanted NFC Tags Using Mobile Phones

ANTONIO LAZARO, (Senior Member, IEEE), MARTÍ BOADA, RAMON VILLARINO, AND DAVID GIRBAU, (Senior Member, IEEE)

Department of Electronic, Electric and Automatic Engineering, Universitat Rovira i Virgili, 43007 Tarragona, Spain

Corresponding author: Antonio Lazaro (antonioramon.lazaro@urv.cat)

This work was supported by the Spanish Government Project RTI2018-096019-B-C31 under Grant BES-2016-077291.

ABSTRACT In this paper we study the read range of implanted sensors based on batteryless, Near-Field Communication (NFC) integrated circuits (IC) using an NFC-equipped smartphone as a reader. The most important challenges are the low coupling between loops of different sizes, the limited quality factor imposed by the bandwidth communication, the effects of the body on propagation, and the detuning of the antennas. Two systems are analyzed: a conventional system based on resonant coupling between two coils; and a system based on resonant coupling between three coils. With the latter, a relay antenna is attached to a patch, which is adhered to the skin. Simulations and measurements show that the quality factor of both antennas can be improved by including a spacer made of low-permittivity material. A circuit model is proposed for the implanted and relay antenna, which simplifies its usage in circuit simulators. Some implanted and relay antenna prototypes are analyzed and a system model that includes a nonlinear model of the tag is used to analyze the maximum depth at which the implant can be read. Our experimental results show that the system based on three coils performs much better performance at longer distances and is more robust to misalignments between coils. A 15×15 mm-implanted tag with commercial NFC IC and energy harvesting can be read using commercial smartphones. It can feed sensors at a distance of up to 16 mm inside the body and at a distance of 3 cm from the skin. Our results also show that data previously stored in the IC memory can be transferred to the reader located at distances of up to 2 cm and 3.8 cm for the 2-coil and 3-coil systems, respectively. This study demonstrates the potential of batteryless NFC sensors for biomedical and wearable applications using mobile phones as readers.

INDEX TERMS Batteryless, energy harvesting, Internet of Things (IoT), implantable medical device, near-field communication (NFC), radiofrequency identification (RFID), wireless power transfer (WPT).

I. INTRODUCTION

Implantable devices are enjoying increasingly widespread acceptance and becoming ever smaller and more powerful [1], [2]. Such devices include implantable glucose and oxygen sensors for diabetics [3]–[5], implantable chemical devices [6], [7], neural implants [8], [9], cochlear implants [10], ocular implants [11]–[13] and cardiovascular devices [14]. Advances in semiconductor technology, particularly in micro-electro-mechanical systems (MEMS), have made it possible to reduce dimensions and increase the number of sensors it is feasible to implant [10]. However, despite recent technological progress in implant technology, many challenges remain unsolved [10]. One of the most critical of these challenges is the power source needed by electronic devices. Rechargeable batteries can be periodically transcutaneously recharged using wireless telemetry, whereas single-use batteries require surgical removal to replace them. To increase biocompatibility (which is associated with battery toxicity) and the lifetime of these devices, batteryless devices are preferred [15]. Although promising communication methods based on ultrasound [16], [17] have been proposed, radiofrequency (RF) is the most widely used communication method. However, the tissues surrounding the implant present dielectric losses that heavily attenuate the electromagnetic signals, thus degrading communication. The read-range and size constraints imposed by the limited space available inside the body are therefore fundamental challenges.

The associate editor coordinating the review of this manuscript and approving it for publication was Chunsheng Zhu.

Although several methods of wireless power transfer (WPT), such as inductive, optical [18] and ultrasound [19], are proposed in the literature, the most established way to power batteryless devices is to use radiofrequency electromagnetic waves [1], [20]–[22].

RFID (Radio Frequency Identification) [23] is a well-known wireless technology for traceability, logistics and access control and is recognized as a key technology for developing the Internet of Things (IoT). In recent years RFID technology has become much more widespread. Traditional barcodes are being replaced by low-cost RFID tags for tracking items. Within RFID technology, several types, including LF, HF or UHF stand out depending on their frequency band. The advantages of tags operating at UHF include their long read range and their low cost in logistics chains. Although the tags are often designed to work in a single RFID band, dual HF and UHF RFID tags have recently been proposed [24]. One that has seen huge growth is near-field communication (NFC) technology, which is a short-range RFID that enables communication between devices using the ISM 13.56 MHz RFID band [25]. Although NFC technology has existed for over a decade [23], [25], it did not become popular until it was massively incorporated into payment systems. NFC technology enables simple and safe communication between electronic devices, allowing consumers to perform contactless transactions, access digital content and connect electronic devices with a single tap. For this reason, most smartphones currently incorporate an NFC reader. The importance of NFC systems within the IoT scenario and Industry 4.0 is, therefore, increasing [26]. NFC technology is also useful for developing low-cost low-range sensors since it provides a fast and easy way to obtain data from them simply by bringing the reader closer to the tag without needing to pair the devices. The biggest NFC integrated circuit (IC) manufacturers have also commercialized NFC IC with energy-harvesting capability that can provide energy to small sensors and microcontrollers [27]–[30].

Traditional WPT between the reader and the implanted device is often performed with a specific design using discrete components or integrated circuits with embedded sensors. Due to size constraints, the dimensions of the implanted coil need to be as small as possible. However, the maximum coupling is obtained for coils of similar size [25], [27] and the NFC readers in conventional smartphones are designed to read smart cards rather than miniature implanted coils. In medical applications, therefore, special readers are required for implanted sensors. The aim of this paper is to study the possibility of working with conventional NFC integrated circuits with energy harvesting that are available on the market [27] (so a specific ASIC does not need to be designed) in implanted devices using the smartphone as a reader. To do so, we present a method for increasing the read range of implanted NFC sensors with energy-harvesting capability based on a 3-coil resonant system and using smartphones as readers. Although multiple resonant coils in WPT applications are proposed in the literature [20], [21], these systems have rarely been used with commercial RFID. As well as transferring power to the implanted device, the NFC system can be used to send data to and receive data from the implant, thus creating a two-way data link. A fast data-rate can also be achieved (e.g. 26 kbps under ISO 15693-compliant IC). To our knowledge, this is the first time that a commercial NFC IC combined with a 3-coil system has been used for implanted devices. Using a standardized system such as the NFC offers further advantages for the commercialization of implanted devices, thus reducing time to market. The number of applications associated with this technology is limited by its inherently short range. However, implanted devices based on NFC sensors may be useful for future implanted glucose sensors, other implanted chemical sensors, and neuroprotheses. This study verifies the potential of batteryless sensors based on NFC technology for novel implanted biomedical and wearable applications using mobile phones as readers.

Wireless communication with implantable medical devices (IMDs) is fundamental for monitoring and reducing surgical operations [31]. However, data transmitted wirelessly can be accessed by nearby third parties [32], [33]. Despite the advantage of this technology, therefore, privacy must be taken into account and safety issues must be addressed [33]. Currently, the main application of NFC tags is for making payments [34]. It can, therefore, be considered a secure system. In addition to the short read range, which provides a certain degree of security, NFC messages can also be protected by a password known only to authorized users, and data can be encoded by the microcontroller included in the implant. Moreover, advanced security protocols can be implemented to improve security [35]. This is a potential advantage of NFC-based IMDs over custom wireless communication systems with a lower degree of security and wireless communication systems with a higher read range.

Despite the potential of NFC technology, there are not previous studies on the maximum depth at which a device can be implanted, being able to feed sensors from the energy harvested from a mobile phone. In this work, the conventional 2-coil and a 3-coil resonant system are compared in terms of read range. In the 3-coil system, the relay coil is integrated on a flexible patch, which is attached on the skin. A new comprehensive model for the implanted and relay antenna that takes into account the effect of body on the coils is developed. An overall system model to analyze the read range is proposed. The analysis considered in previous works proposed in the literature (eg. [20]) is based on a linear analysis that includes the effect of coupling between the coils and the frequency, consisting of using a simplified model of the antennas that does not consider the nonlinear tag behavior. This work uses a commercial circuit simulator to include a model of the main blocks of the NFC IC. In the literature, the simplified linear analysis of the WPT is often compared to measurements of efficiency made from a vector network analyzer. However, these measurements are not often performed with a real reader and the load is simulated with a constant value, which is far from the real case, since this

is a function of the received power. Another effect such as the detuning of the coils by the presence of the metal case of the mobile is not considered in former works. An automated experimental setup to compare the 2-coil and the 3-coil systems using phantoms has been developed. A commercial smartphone is used as a reader in this setup. The setup is based on the measurement of the average magnetic field received in the tag, which depends on the transmitted power, the coils and coupling between coils. Therefore, this measurement is performed in a real scenario and it takes into account the detuning effect, which is difficult to be modeled because it depends, among other parameters, on the distance or the reader antenna integration in the mobile. The read range is determined when the average magnetic field is higher than a minimum magnetic field that is a function of the NFC IC and the coil used in the tag. Therefore, its value can be interpreted as a figure of merit of the implanted tag. The former concepts are used in the certification of NFC systems but have not been applied to analyze the performance of implanted HF tags. Although the read range can be also limited by the data transmission by backscattering, experimental results with an implanted sensor will show that the main limitation is energy harvesting.

The paper is organized as follows. Section II describes the systems based on 2 and 3 coils for wireless power transfer and reviews some basic theory related to the efficiency and power delivered in these systems. Section III analyzes the various parts of the system (transmitter, NFC IC model, and effects of the body on antennas), and presents simulations of the efficiency, the power delivered, the typical coupling between the antennas, and the read range that can be achieved. Section IV presents our experimental results for the 2-coil and 3-coil systems. Finally, Section V contains a summary and the conclusions of our work.

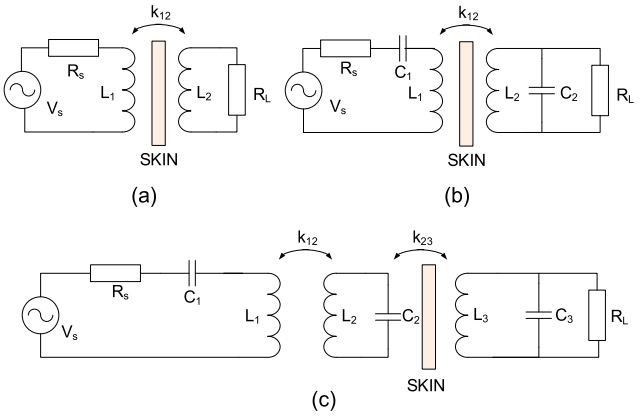

FIGURE 1. (a) Non-resonant inductive link, (b) resonant coupling with 2 coils, and (c) resonant coupling with 3 coils.

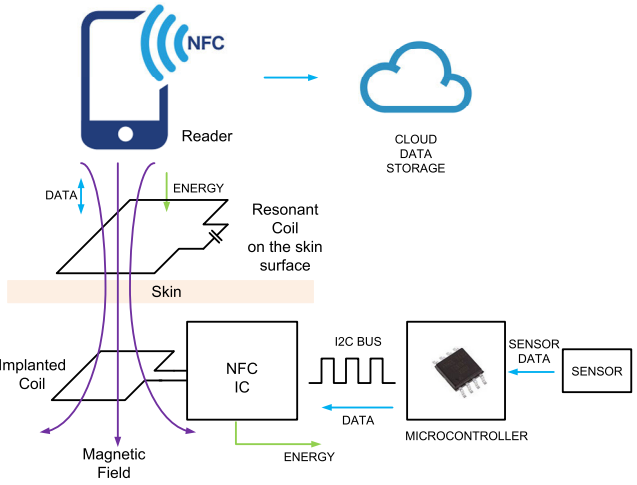

FIGURE 2. Schema of the proposed system with 3 coils.

II. SYSTEM OVERVIEW

Although both electric and magnetic fields can be used for power transmission, most applications adopt magnetic field transmission because it is less influenced by the high permittivity of the body. Moreover, magnetic coupling is easy to implement with loop antennas. The usual way to transfer power through biological tissues is by magnetic induction. A typical wireless power transfer system consists of a power source, a transmitter coil, a receiver coil and a load [21] (see Fig.1). Communication by inductive coupling is carried out between two coils and has the advantage of being more efficient than far-field communication. Since there is no difference in permeability between the body tissue and the air, the magnetic field does not encounter any boundary conditions [21]. The main drawbacks with magnetic coupling are that its efficiency is extremely sensitive to primary-secondary coil alignment and distance beyond the near-field region, where the magnetic field quickly decays as $1/d^3$ from the source coil, with d being the distance between coupled coils. When the implant is much smaller than d, the coupling between the coils is weak. Inductively coupled coils operating in this weakly coupled regime are usually very inefficient. The limitations in distance and alignment accuracy can be solved by systems addressed as resonant magnetic coupling [36], [37]. Fig.1a shows a circuit schema for non-resonant inductive coupling, while Fig.1b and Fig.1c show resonant coupling with 2 and 3 coils, respectively. Inserting a relay coil between the source and the load introduces a degree of freedom that improves the system. Fig. 2 shows the system using 3 resonant coils as proposed in this paper. The system is based on a smartphone with an integrated NFC reader, a relay coil located on the surface of the body, and the implanted NFC tag. Since using the relay coil inside the body would increase the size of the implant, it is placed on the skin outside the body. Another way to improve the WPT would be to use a system with 4 coils. However, with this topology, both the second relay coil and the load coil would need to be implanted, which would increase the size of the implant and make the system impractical.

The main requirement in the proposed biomedical link is to deliver sufficient power to the load to activate the electronics with high-power transfer efficiency (PTE). Achieving this is

challenging when the distance between the transmitter and the receiver is large or the coils are not aligned.

Efficiency, defined as the ratio between the load power delivered and the input power, can be computed from the S_{21} parameter using the source (R_S) and the load resistance (R_L) as reference impedance in the S-parameter calculation. The efficiency and load power delivered for multiple resonant WPT have been studied in the literature [20]. Analytical expressions at the resonant frequency when all the LC resonators are tuned to the same frequency can be obtained for a 2-coil (1) and a 3-coil system (2) [20]:

$$\eta_{2coils} = \frac{P_L}{P_{in}} = \frac{k_{12}^2 Q_1 Q_{2L}}{1 + k_{12}^2 Q_1 Q_{2L}} \cdot \frac{Q_{2L}}{Q_L} \tag{1}$$

$$\eta_{3coils} = \frac{k_{12}^2 Q_1 Q_2}{1 + k_{12}^2 Q_1 Q_2 + k_{23}^2 Q_2 Q_{3L}} \cdot \frac{k_{23}^2 Q_2 Q_{3L}}{1 + k_{23}^2 Q_2 Q_{3L}} \cdot \frac{Q_{3L}}{Q_L} \tag{2}$$

In (2), the coupling between the first and the last coil is neglected since they are a long away from each other. The power delivered at load P_L for the two cases is given by:

$$P_{L,2coils} = \frac{V_S^2}{2R_1} \cdot \frac{1}{1 + k_{12}^2 Q_1 Q_{2L}} \cdot \eta_{2coils} \tag{3}$$

$$P_{L,3coils} = \frac{V_S^2}{2R_1} \cdot \frac{\left(k_{12}^2 Q_1 Q_2\right) \cdot \left(k_{23}^2 Q_2 Q_{3L}\right)}{\left(1 + k_{12}^2 Q_1 Q_2 + k_{23}^2 Q_2 Q_{3L}\right)^2} \cdot \frac{Q_{3L}}{Q_L} \tag{4}$$

where the unloaded quality factor of each coil is obtained from the coil inductance and resistance at angular resonance frequency ω_0:

$$Q_i = \frac{\omega_0 L_i}{R_i} \tag{5}$$

where $i = 1, 2, 3$. The loaded quality factor is computed from:

$$Q_{iL} = \frac{Q_i Q_L}{Q_i + Q_L} \tag{6}$$

and the external quality factor is given by:

$$Q_L = \frac{R_L}{\omega_0 L_{end}} \tag{7}$$

where $L_{end} = L_2$ for the 2-coil system and $L_{end} = L_3$ for the 3-coil system.

The optimal coupling coefficient k that maximizes the power delivered to the load (PDL) (3)-(4) and the efficiency (PTE) (1)-(2) are obtained from [20] by differentiation of the equations:

$$k_{12,PDL,2coils} = \frac{1}{(Q_1 Q_{2L})^{1/2}} \tag{8}$$

$$k_{12,PDL,3coils} = \left(\frac{1 + k_{23}^2 Q_2 Q_{3L}}{Q_1 Q_2}\right)^{1/2} \tag{9}$$

$$k_{23,PDL,3coils} = \left(\frac{1 + k_{12}^2 Q_1 Q_2}{Q_2 Q_{3L}}\right)^{1/2} \tag{10}$$

$$k_{23,PTE,3coils} = \left(\frac{1 + k_{12}^2 Q_1 Q_2}{Q_2^2 Q_{3L}^2}\right)^{1/4} \tag{11}$$

Maximum delivered power and maximum efficiency cannot be satisfied simultaneously [20]. Given that batteryless implants are considered in this work, the tag can only be powered in the presence of a mobile phone. The main goal, therefore, is to ensure that the NFC IC receives enough power or AC voltage to enable the correct rectification for feeding the sensors and the other electronics in the implant, unlike other WPT systems used to charge batteries, where efficiency is fundamental. In addition, optimum couplings are often outside the typical values in an implanted system and depend on the distance, coil alignment, antennas used in the reader (which vary according to the model of smartphone), and implanted antennas. Another important aspect not considered in the literature is that the load impedance and loaded quality factor depend on IC impedance. The IC impedance, therefore, depends on the power received and presents nonlinear behavior [38]–[40]. This nonlinearity must be taken into account in both the simulations and the system design. Simple linear network simulations are not sufficient, so more complex nonlinear simulation methods must be used. Due to the nonlinear behavior of the NFC IC, therefore, (1)-(4) cannot be used since the load resistance (R_L), which depends on the received power, is unknown. To perform accurate simulation of the systems, in the following sections we analyze the various parts of the WPT system. The overall system can be analyzed using circuit simulators such as Keysight ADS. We have carried out harmonic balance nonlinear simulations with this circuit simulator.

III. SYSTEM ANALYSIS

In this section, we model the various parts of the system before they are introduced into the circuit simulator and present the system simulations at the end of the section. The read range of the device powered by the reader in a smartphone is also theoretically and experimentally analyzed. First, we describe the transmitter model and the NFC tag IC model used in the simulations before studying the effect of body materials on the implanted and relay antennas. We also analyze the coupling between the smartphone reader and the tag antennas to obtain the maximum depth of the implant. Finally, we conduct simulations of wireless power transfer performances.

A. TRANSMITTER

Unlike previous works in which a specific transmitter and receiver for a medical WPT were used, in this paper, we propose using the smartphone as a transmitter to read standardized NFC tags that are subcutaneously implanted. The reader cannot, therefore, be modified, and the NFC antenna depends on the smartphone used. In modern smartphones, the NFC antenna is often integrated with a ferrite layer on top of the battery [41]–[44] in phones with plastic cases, or around the camera in phones with metallic cases [45]–[50]. As the

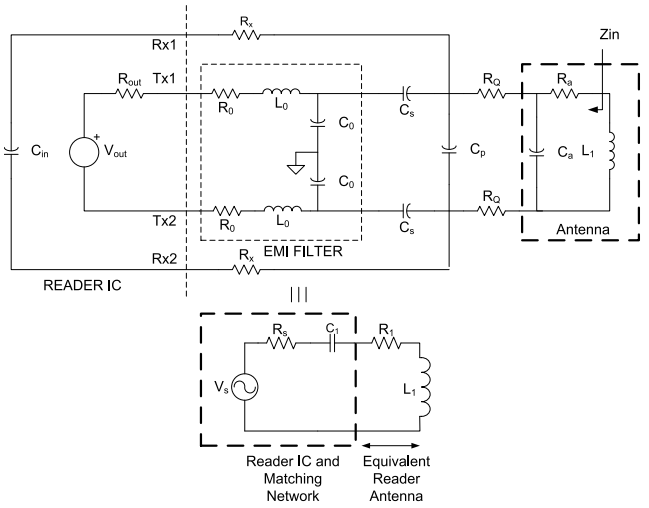

FIGURE 3. Model of the reader, including the matching network (top) and the simplified model (bottom).

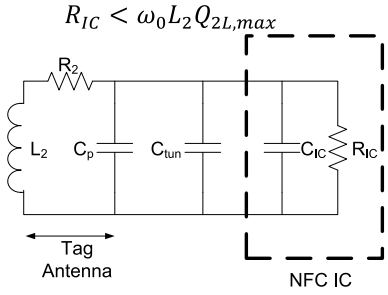

FIGURE 4. Simplified model of the tag including the tag antenna, tuning capacitor and NFC IC.

main application is for making payments, mobile antennas are often optimized to read payment cards (standard size = 85.60 × 53.98 mm). The loop size is approximately a square measuring 3–5 cm wide. A weak coupling can therefore be expected between the reader and the implanted coil with a diameter in the order of 10-15 mm. The coupling between antennas is investigated below.

Other restrictions are imposed for the required bandwidth for NFC communication. To ensure that the communication works properly, the maximum value of the Q factor of the initiator antenna must be such that bandwidth B (at −3 dB), which is equal to f_c/Q, is at least capable of channeling all the frequencies contained in the spectrum of the signal modulating the carrier frequency, $f_c = 13.56$ MHz. The bandwidth of the forward link is the bandwidth of the modulation sidebands of the carrier. The maximum loaded Q of the transmitter is given by $f_c \times T_p$, where T_p is the pause time on the carrier modulation. According to NFC forum standard ISO 14443, the quality factor is limited to 40 (35 if we consider design tolerances) at 106 kbit/s bit-rate transfers [25]. For applications that use ISO 15693, whatever the bit rate, the shortest time present in the uplink communication protocol is a 'pause' lasting $T_p = 9.44$ μs. In this case, $Q_{1max} = 128$, which can generally be reduced to a usable value of 100, assuming design tolerances. As smartphones are designed to read a variety of NFC protocols, the quality factor is limited to 35 [24], [26]. Generally, these values of usable Q_{1max} are not difficult to obtain and are easy to reduce using a serial resistance (R_Q in Fig.3).

Fig.3 shows the schema of the transmitter with the matching network and the EMI filter. In some applications, it is known that the reader communicates correctly with a smart card at long distances but not at short distances, irrespective of the (good) demodulation quality of the backscattered signal [51], [52]. This phenomenon is known as the loading effect and results in a lack of transmitted power due to the strong influence of the tag's load on the reader [51], [52]. The presence of metallic materials close to the loop antenna leads to a reduction in the inductance and the detuning of the transmitter. High dielectric permittivity materials (e.g. the proximity of the body) increase parasitic capacitance, so some detuning effect is expected due to the change in the antenna's resonance frequency. These detuning effects and the over-coupling introduce a restriction in the minimum distance to the relay coil.

To insert the transmitter into the circuit simulator, a simplified model is used (Fig.3). The reader can be modeled using a Thevenin equivalent circuit with a voltage source and an output impedance, R_s. A series capacitance C_1 is added to make the circuit resonant at the operating frequency. The parasitic capacitance of the reader antenna has been taken into account in the matching network. An equivalent model can be used for the reader antenna, which is modeled as an inductance (L_1) and its losses R_1 (including R_Q to set the reader quality factor Q_1) in series with the inductance. The reader includes a matching network, so a perfect match is assumed at the resonance frequency, $R_s = R_1$. The parasitic capacitance of the reader antenna has been taken into account in the matching network and is included in the equivalent Thevenin model.

The final consideration is that, unlike with other WPT systems, when a smartphone is used as an NFC reader, the transmitted power and reader antenna topology depend on the mobile model. The typical transceiver IC for NFC in commercial smartphones can achieve transmitted powers of 20–23 dBm (e.g. NXP PN7120 or TI TRF7970A IC transceivers).

B. NFC TAG IC MODEL

A simplified model for the tag is shown in Fig.4. NFC IC impedance is nonlinear and depends on the power received. The tag is modeled as a resistance (R_{IC}) in parallel with a capacitor (C_{IC}). A tuning capacitance C_{tun} is added to make the circuit resonant at the operating frequency. Most studies on WPT focus on optimizing the system as a function of the quality factor of the coils, the coupling, and the load resistance. However, the wireless power transfer in NFC RFID systems also imposes certain restrictions on the receiver [25], [27]. Analogously to the case of the transmitter,

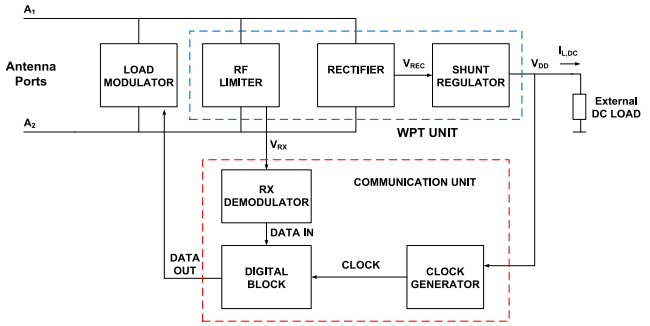

FIGURE 5. Block diagram of the NFC tag IC.

the quality factor in the tag (Q_{2L} for the 2-coil system and Q_{3L} for the 3-coil system) is limited to prevent degradation in the modulation of the subcarrier. The maximum value of Q_{2L} is therefore approximately $Q_{2L,max} = 8\pi \approx 25$ [53]. A higher quality factor would increase the time constants for the transition and decrease the load modulation. This limitation is not often considered in medical inductive links because such systems usually use lower transmission rates than NFC RFID systems, and it is not present in WPT systems devoted to wireless charging. The tag quality factor is given by the hyperbolic average of the quality factor of the tag antenna and the quality factor associated with IC impedance (6)-(7). Therefore, given an implanted inductance L_2 in the order of 0.7 μH, the R_{IC} must be lower than roughly 1500 Ω in order to achieve the communication bandwidth for the backscattering link:

$$R_{IC} < \omega_0 L_2 Q_{2L,max} \tag{12}$$

To estimate the performance of the energy harvesting, we conducted a system simulation using a Keysight ADS simulator and a harmonic balance simulation method. This requires a nonlinear model for the IC tag. Details of the hardware implementation of the IC are needed but these data are not available for users. Fig.5 shows the main block of an NFC tag IC. Two main blocks are connected to the antenna [54]. The first of these is the wireless power transfer unit in charge of energy harvesting to power up the IC, while the second is the communication unit that demodulates the data and generates the clock for transmitting information back to the reader. In this paper, we focused on the WPT unit. This is made up of an RF limiter, a rectifier, a shunt regulator and a load modulator, which can be modeled as a shunt capacitance with the antenna.

Because of its proximity to the reader, the coupled AC signal at the antenna can be large, which may cause the destruction of the MOS transistor. An RF limiter is therefore needed to prevent damage to the internal circuit from any undesired high-input signal. After this limiting step, the AC signal is translated into a DC signal by means of a full-wave rectifier. The rectified DC voltage is regulated to obtain a stable voltage for the communication unit operation.

To model the limiter, we used the circuit described in [54] and shown in Fig.6a. This limiter is based on two large-area

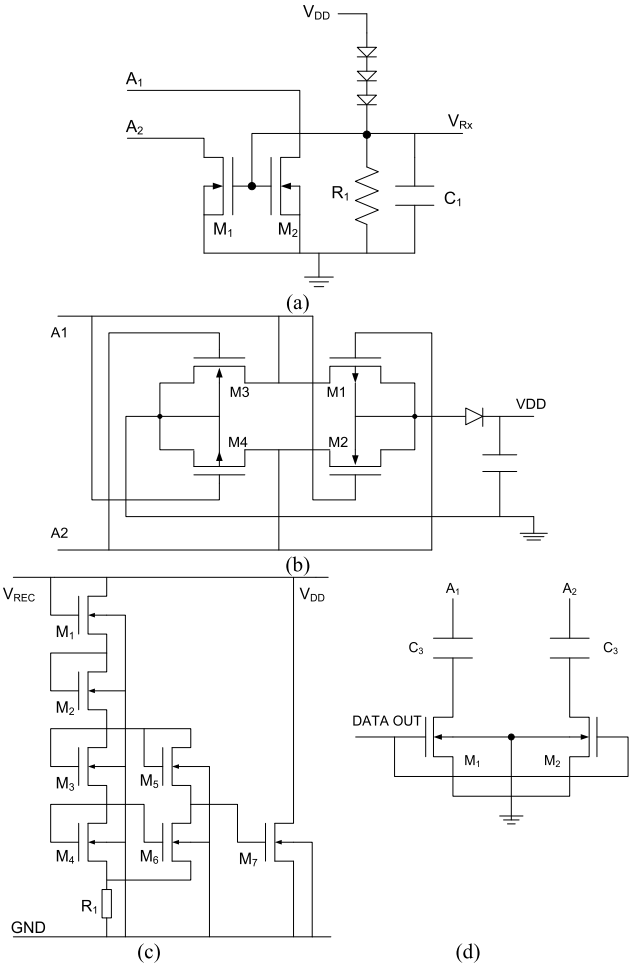

FIGURE 6. Main block circuits of the WPT unit of an NFC tag IC: (a) RF limiter, (b) full-wave rectifier, (c) shunt regulator, and (d) load modulator.

NMOS shunt transistors that are activated when the input power is sufficient to produce a current through the diodes that is larger than the threshold voltage needed to activate the transistors. The limiter is also used to implement an envelope detector using the diodes and the R_C filter (R_1 and C_1) for ASK demodulation. The output of this circuit V_{Rx} is used as the input of a slicer circuit for data demodulation.

A high-efficiency rectifier is required for RF-to-DC conversion. This is often based on a full-wave bridge rectifier in which the diode pairs turn on during each cycle of the AC signal. However, efficiency is limited by the threshold voltage of the diodes. Schottky diodes can be used in this topology to reduce these voltage drops, but these devices are not compatible with conventional CMOS technology. Several CMOS-based rectifiers have been proposed in the literature. Those most often used are the NMOS bridge and the CMOS gate cross-coupled (or cross-connected) rectifier [55]. The rectifier used in the simulations is based on the CMOS gate cross-coupled rectifier (Fig.6b). This topology presents a lower turn-on level than an NMOS bridge.

A shunt regulator can be used to model the regulator in the simulation (for example, based on a Zener diode). Although

TABLE 1. Dielectric layers used in the simulation of the body at 37°C.

Layer	Relative permittivity	Conductivity (S/m)	Thickness (mm)
Skin (epidermis+dermis)	120	0.25	1.5
Fat (hypodermis)	38	0.21	4
Muscle	138	0.62	25

lateral Zener diodes can be implemented in standard CMOS processes [56], the shunt regulator is often implemented with transistors. However, all topologies are based on the same principle, which involves reducing the shunt resistance of a bypass transistor when the input voltage is below the desired output voltage. Fig.6c shows the shunt regulator used here [51], [57], [58]. In this circuit, the shunt impedance to reduce the voltage is controlled by comparing a band-gap-based reference voltage and the output voltage.

The load modulator (Fig.6d) is made up of two NMOS transistors that act as switches, each of which connects one capacitor from the RF input to the ground [59], [60]. To transmit information to the reader, the transistors are switched on and off by the data signal connected to the gate, which results in a change of load impedance at the antenna as a function of the data. Since this work focuses on the WPT, in the circuit simulation the effect of the modulator is included in the shunt parasitic capacitance of the IC. The nonlinear model is implemented in Keysight ADS using the TSMC 0.18 μm CMOS design kit from MOSIS [61].

C. EFFECT OF THE BODY ON THE IMPLANTED ANTENNAS AND MODELING

The effects of the body, due to the antenna being close to the skin surface (relay coil) and the antenna being implanted, must be taken into account. The epidermis (the outermost layer of skin), which has a thickness of roughly 100 μm, provides a waterproof barrier. The dermis (which lies beneath the epidermis) contains tough connective tissue, hair follicles, and sweat glands. The dermis is roughly 1–2 mm thick but this thickness in the same body area can vary significantly with age [62], [63]. The deeper subcutaneous tissue (hypodermis) is made up of fat and connective tissue. Its thickness varies from 1 to 15 mm. Below the fat is a layer of muscle. Fig.7 shows a schematic cross-section. Table 1 shows the dielectric permittivity and conductivity of tissue material at 13.56 MHz, taken from the literature [63]–[66], which are used in the electromagnetic simulator (Keysight Momentum) to simulate the body.

WPT at 13.56 MHz requires coils of the order of 0.5-1 μH. A small number of turns is therefore needed to reach this inductance. The antenna can be implemented using wound wires, multistrand wires (Litz wires) or printed loops [2]. In this study, only printed antennas were considered because they easily allow the connection of integrated circuits or other electronics. Although square printed antennas have been used, other shapes or loops with wires could also be considered. Analytical expressions for estimating inductance for typical shapes from the coil dimensions are available in the literature [67], [68]. However, to calculate the antenna's parasitic elements, include the effects of via holes, or consider the exact layout of the antenna, electromagnetic simulators are often required. To study how the body affects the antennas, we considered two cases: implanted antenna (section C.1) and relay antenna on the skin surface (section C.2).

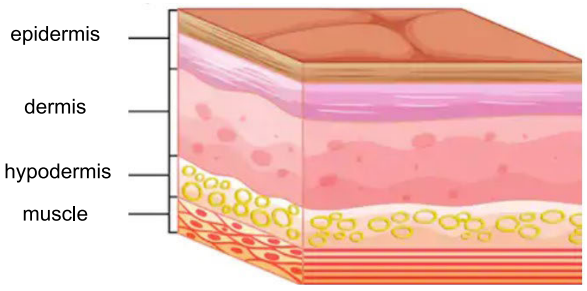

FIGURE 7. Skin cross-section.

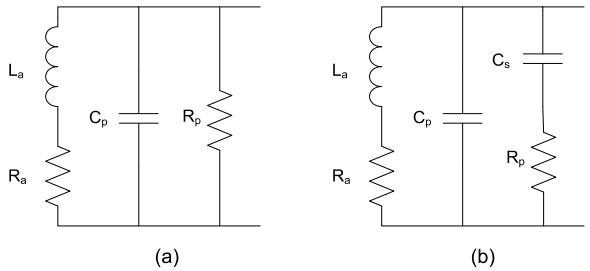

FIGURE 8. (a) Circuital antenna model for a loop antenna in the air, and (b) improved circuit model proposed for an implanted loop antenna.

1) IMPLANTED ANTENNA

Fig.8.a shows the circuit model commonly used for a loop antenna in the air. It is important to note that inductance (L_a) is not affected by the dielectric substrate and is therefore unaltered when the antenna is implanted in the body. However, parasitic capacitance (C_p) increases due to the high permittivity of bodily matter, so the tag's resonance frequency also increases. Dielectric losses can be modeled by adding a resistance in parallel to the antenna (R_p in Fig.8a). This resistance is parallel to the load, thus reducing its value and degrading the quality factor.

Implantable devices need to be encapsulated to prevent contamination and protect the electronic or mechanical systems. Implantable silicone materials can be used inside the body for long periods of time, depending on the needs of the medical device and the limitations of the material chosen [69]. Silicone rubber is normally chosen for implantable devices due to its high chemical inertness and durability. Implantable grades of silicone are not rejected by the body and do not cause infection since they are biocompatible for use in humans. Coating the implanted antenna has a significant influence on its properties. The spacer (h_c) introduced by the coating isolates the antenna from the losses intro-

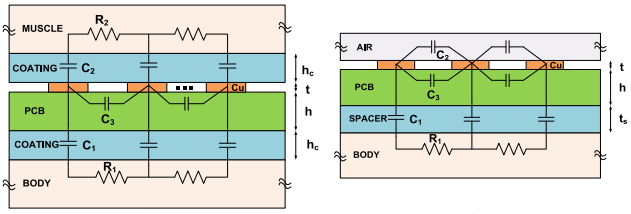

FIGURE 9. **(a) Cross section of a subcutaneously implanted antenna and (b) cross section of the relay antenna on the body.**

duced by the body (muscle). Consequently, a reduction in detuning and a noticeable increase in the quality factor are expected compared to when the antenna is used without coating. An improved equivalent circuit for the implanted antenna is proposed to take into account these effects (Fig.8b). The different contributions of the multilayer dielectric structure need to be analyzed to obtain this lumped equivalent circuit. Fig.9a shows a simplified cross section of the implanted antenna surrounded by the coating material. This material is a low-loss dielectric (silicone) that introduces a series capacitance between the metal strips of the printed loop and the muscle material (C_2 in Fig.9). In the simulations, we considered the dielectric properties of the silicone to be $\varepsilon_r = 3$, $\sigma = 2.26{\cdot}10\text{-}6$ S/m, and $\tan\delta = 0.001$. The material also introduces resistance due to its low conductivity. This distributed RC network can be modeled as an equivalent resistance (R_1) in series with a capacitance (C_1). Finally, a parasitic capacitance in parallel can be introduced to model the capacitance between the strips (C_3).

The components of the distributed circuit in Fig.9 are difficult to obtain. A simplified lumped equivalent circuit (Fig.8b), where the elements can be obtained from electromagnetic simulations or measurements, is therefore more useful. The resistor (R_a) in series with the inductor gives a quality factor that increases with frequency, while the resistor (R_p) in parallel with the inductor gives a quality factor that decreases with frequency. A combination is therefore widely adjustable to produce a peak in the quality factor at any arbitrary frequency. The equivalent capacitance C_s takes into account the distributed capacitances of the coating layers.

The series antenna resistance (R_a) is frequency-dependent, mainly due to the skin effect. The conductivities of biological tissues are much lower than those of the metal used for the coil strips, so the eddy-current generation in the tissue is insignificant. The series antenna resistance can be computed from [70]:

$$R_a = R_{dc}\frac{t}{\delta\left(1-e^{-t/\delta}\right)}\cdot\frac{1}{1+t/W} \tag{13}$$

where DC resistance R_{dc} is given by;

$$R_{dc} = \frac{L}{\sigma W t} \tag{14}$$

and skin depth δ is:

$$\delta = \frac{1}{\sqrt{\sigma\pi f\mu_0}} \tag{15}$$

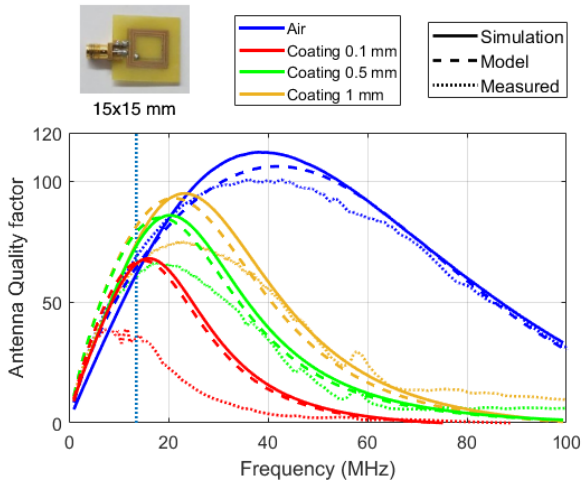

FIGURE 10. **Antenna quality factor as a function of frequency, in the air and implanted, with different coating thicknesses. Continuous line: electromagnetic simulation; dashed line: circuit model (Fig.8a for antenna in air and Fig.8b for implanted antenna). Dotted line: measurements of the antenna.**

In (13-15), L is the length of the strip, t is the thickness of the strip, W is the width of the strip, μ_0 is the vacuum magnetic permeability constant ($4\pi{\cdot}10^{-7}$ H/m), and σ is the conductor conductivity.

Fig.10 compares the antenna quality factors of a printed coil in the air and of one in the body surrounded by muscle tissue and assuming that it has a coating of silicone of different thicknesses. Fig.10 compares the quality factor obtained from the Momentum simulations, the model, and the measurements. The quality factor is computed from the real part and the imaginary part of the input impedance Z using:

$$Q_a = \frac{Im(Z)}{Re(Z)} \tag{16}$$

Permittivity and conductivity are shown in Table 1. The implanted antenna is designed using a 0.8 mm thick FR4 PCB substrate. To miniaturize the design, the antenna is a double-sided loop with 3 turns on each side, a strip width of 0.5 mm, a strip spacing of 0.5 mm, and an external length of 15 mm. These values of width and spacing can be created using standard PCB manufacturing processes whose tolerance ranges from 100 to 150 μm. The antenna presents an inductance of 0.68 μH, which is higher than the value needed to meet the bandwidth specification given by (12). Good agreement is found between the electromagnetic simulations and the circuit model in Fig.8b, which is obtained from optimization using Keysight ADS. R_{dc} is optimized to take into account the exact length L of the antenna. Antenna resistance is computed from (13) using R_{dc}, width W and thickness t. The initial values for C_p and C_s are set to half the value of C_p obtained in the air (extracted from the resonance frequency). The initial value of the inductance is extracted at low frequency from the imaginary part of the impedance. Table 2 compares the cases of the antenna in air and the antenna implanted with several thicknesses of silicone cover. The components of

TABLE 2. Equivalent circuit for the implanted antenna obtained by optimization from electromagnetic simulations.

Parameter	In air	Implanted antenna with different thicknesses of silicone coating		
Thickness of coating (mm)	0	0.1	0.5	1.0
R_{dc} (Ω)	0.38	0.38	0.38	0.38
R_a(Ω)	0.95	0.89	0.78	0.78
f_r (MHz)	135.8	75.1	104.6	120.9
C_p (pF)	2.02	0.93	0.94	0.90
L_a (μH)	0.68	0.68	0.68	0.68
R_p (Ω)		78.5	72.56	192.01
C_s(pF)		7.20	3.45	2.78
Q_a^*(13.56 MHz)	61.4(61.8)	65.9 (35.0)	74.2 (60.5)	73.2 (64.5)
C_{tun} (pF)	201.04	200.18	203.8	143.05

*Quality factors obtained from simulation (the values in parenthesis are obtained from measurements).

the equivalent circuit of Fig.8a (air) and Fig.8b (implanted) are also shown in Table 2. The tuning capacitances C_{tun} that need to be added in parallel for the antenna to become resonant at 13.56 MHz (including the chip capacitance $C_{IC} = 27.5$ pF for the M24LR04E) are also given in this table. The capacitance C_{tun} is computed from the imaginary part of the impedance Z at $f_0 = 13.56$ MHz:

$$C_{tun} = \frac{1}{(2\pi f_0)\, Im(Z\,(f_0))} - C_{IC} \tag{17}$$

The dotted line in Fig.10 shows the measurements of the quality factor for a prototype inserted in a phantom (a piece of pork sirloin). To simulate a flat coating, the antenna is covered by 3D-printed polylactic acid (PLA) layer of various thicknesses and inserted into the meat. The permittivity of the PLA is close to that of silicone ($\varepsilon_r \approx 3$) [71]. The quality factor obtained in the case of the antenna in air is slightly lower than in the simulations. The measurements show that the quality factor improves when the coating thickness increases. These quality factor values are close to 40 for a coating thickness of 0.1 mm and increase to over 63 for a coating thickness of 1 mm. However, the quality factor obtained with the phantom is lower than in the simulations. This is because the conductivity of the meat is higher than that used in the simulations due to the higher content of water and its accumulation in the interface between the meat and the spacer.

We can see that when the antenna is implanted, due to the dielectric permittivity of the tissue, the resonance frequency is lower than when it is in the air. When the thickness of the silicone coating increases, the effective permittivity decreases, so the resonance frequency and the peak frequency of the quality factor increase. The fields are therefore concentrated between the electrodes and the coating material, which leads to a reduction in the losses. The optimum thickness of the silicone cover, around 0.5 mm, maximizes the quality factor.

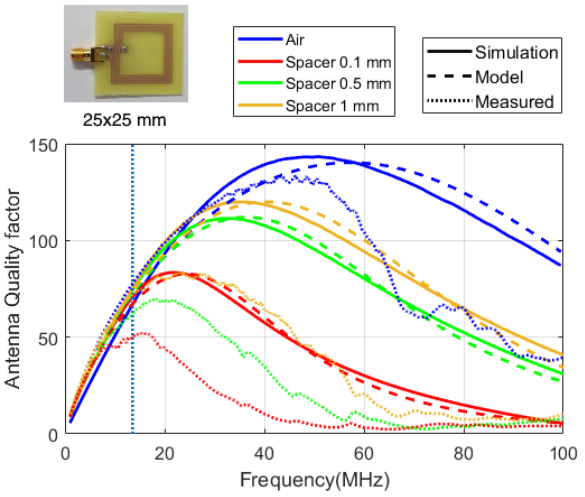

FIGURE 11. Antenna quality factor of the relay loop antenna as a function of the frequency in air and on the skin with different spacer thicknesses. Continuous line: electromagnetic simulation; dashed line: circuit model (Fig.8a for antenna in the air and Fig.8b for implanted antenna). Dotted line: measurements of the antenna.

Although the maximum quality factor is lower than when the antenna is in the air, the peak frequency is closer to the operating frequency. Slightly higher values of quality factor are therefore obtained for the implanted antenna than for the antenna in the air.

2) RELAY ANTENNA ON THE SKIN SURFACE

A similar analysis to that performed for the implanted antenna (section C.1) was conducted for a relay coil placed in contact with the skin (see Fig.9b). The data on stack materials described in Table 1 were also used to simulate the body in the electromagnetic simulations with Keysight Momentum. However, the dielectric properties of tissue and skin vary greatly between individuals depending on the water content of their tissues. One strategy for reducing this effect in the relay – and therefore also in the detuning associated with this variability (which affects the electromagnetic properties of the tissues) is to add a buffer layer with low losses and low permittivity. This coating layer is also needed to protect the electronics, thus preventing short circuits and biocompatibility contamination. Silicone is again proposed in this case because it is a biocompatible material. However, other materials with low permittivity (around 2-3) can be used to integrate the coil into a flexible band-aid for greater breathability.

Fig.11 shows the effect of the silicone spacer layer (thickness t_s) in the antenna model. The prototype relay antenna considered in this study consisted of a square loop (25×25 mm) with 4 turns, a track width of 0.5 mm, and a spacing between tracks of 0.5 mm, printed on FR4 substrate with a thickness of 0.8 mm. When the thickness of the spacer layer increases, the frequency response tends to reach the values obtained for the isolated loop antenna in the air. This antenna presents a higher quality factor in the air than that achieved in the implanted antenna. However, because of the

TABLE 3. Equivalent circuit for the relay antenna obtained by optimization from electromagnetic simulations.

Parameter	In air	Implanted antenna with different thicknesses of silicone coating		
Thickness of coating (mm)	0	0.1	0.5	1.0
R_{dc} (Ω)	0.43	0.42	0.42	0.42
R_a(Ω)	0.98	0.98	0.98	0.98
f_r (MHz)	173.3	113.5	140.3	150.0
C_p (pF)	2.0	0.07	0.07	0.07
L_a (μH)	0.70	0.70	0.70	0.70
R_p (Ω)		790.7	685.9	727.3
C_s(pF)		1.0	0.5	0.4
Q_a*(13.56 MHz)	61.7 (77.8)	69.9 (49.4)	74.2 (58.5)	74.0 (62.1)
C_{tun} (pF)	194.8	196.7	196.7	196.7

* Quality factors obtained from simulation (the values in parenthesis are obtained from measurements).

substrate height and the spacer thickness up to the skin, the quality factor remains roughly constant at around 75, which is close to the value in the air.

Agreement is good between the simulated model and the improved model in Fig.8b, which models the quality factor. The parameters of this model, which are fitted by optimization using Keysight ADS optimization tools to match the antenna's frequency impedance, are shown in Table 3. The dotted line in Fig.11 shows the measurements of the quality factor of a prototype relay coil in the air and on a phantom. This phantom is a piece of pork sirloin with a spacer made of PLA. As with the implanted coil, the values of the quality factor are smaller than those from the literature, whose parameters are used in the simulations, mainly because of the higher water content in the meat. However, the improvement due to the increase in the spacer thickness is clearly perceptible and close to the value in the air. The quality factor increases from 40 for a spacer of 0.1 mm to 73 for a spacer of 2 mm.

D. COUPLING BETWEEN ANTENNAS

As well as restrictions in the maximum quality factor, in NFC RFID systems based on smartphones, the coupling coefficient between antennas also depends on distance, the alignment between antennas, and the type of antenna embedded in the mobile. Since biological materials are non-magnetic, the coupling between antennas is largely the same as in the air. The coupling coefficient is needed to estimate the maximum depth of the implant for a given distance between the body and the smartphone. The coupling coefficient k between two coils can be calculated from the Z parameters obtained from the S parameters:

$$k = \frac{\sqrt{Im\,(Z_{12}) \cdot Im\,(Z_{21})}}{\sqrt{Im\,(Z_{11}) \cdot Im\,(Z_{22})}} \tag{18}$$

Several loop antennas were manufactured on 0.8 mm thick FR4 substrate with a track width of 0.5 mm, and the coupling between them was measured. The distance between

TABLE 4. Sizes of antennas used in the coupling study.

Antenna name	Dimensions	Number of turns	L_a (nH)	R_a (Ω)
Implanted	15 mm × 15 mm	6	666	0.83
			684*	0.91*
Relay 1	25 mm × 25 mm	4	697	0.98
			716*	0.98*
Relay 2	25 mm × 25 mm	6	1185	1.12
			1172*	0.99*
Reader 1	25 mm × 25 mm	4	697	0.98
			716*	0.98*
Reader 2	25 mm × 25 mm	6	1185	1.12
			1172*	0.99*
Reader 3	50 mm × 50 mm	4	2965	2.39
			2893*	2.89*

Simulated and measured (*) inductance (L_a) and resistance (R_a) at 13.56 MHz

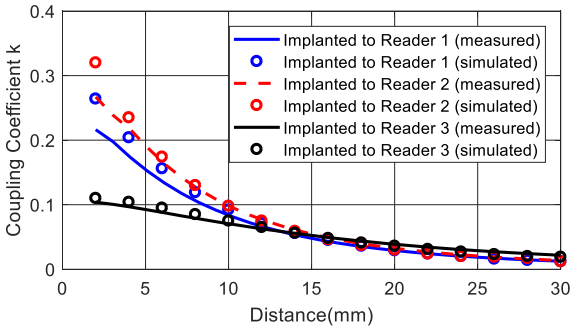

FIGURE 12. Simulated and measured coupling coefficients between the implanted antenna and reader antennas described in Table 4.

the coils was changed using a linear actuator controlled by a stepper motor. The nomenclature and main parameters of the antennas (inductance and resistance at 13.56 MHz) are described in Table 4. This table also compares the simulated and measured inductance and resistance at 13.56 MHz. Small differences were found due to the PCB tolerances. The implanted antenna consisted of a double-sided 15×15 mm square loop with 6 turns. Two relay antennas (Relay 1 and Relay 2) measuring 25×25 mm with 4 and 6 turns, respectively and three antenna sizes for the reader were analyzed. The size of the reader 1 and reader 2 antennas were similar to those integrated around cameras in smartphones, which is the typical position for mobiles with metallic cases [29]. The size of reader 3 antenna, on the other hand, was similar to that of antenna in the battery case for smartphones with plastic cases. In [29], the authors showed that the ferrite material used to isolate the coil from the battery or other metallic parts has a small influence on the coupling coefficient. The following simulations and measurements were therefore performed in the air.

Fig.12-14 compare the simulations and the measurements with Vector Network Analyzer (VNA) of the coefficients obtained using (16) from S parameters as a function of the distance between coils. The coupling coefficient (k_{12}) between

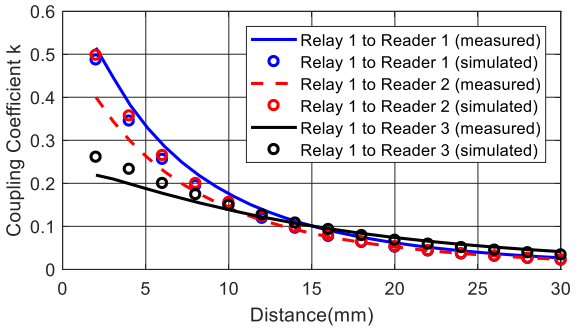

FIGURE 13. Simulated and measured coupling coefficients between the relay antenna (Relay 1) and different reader antennas described in Table 4.

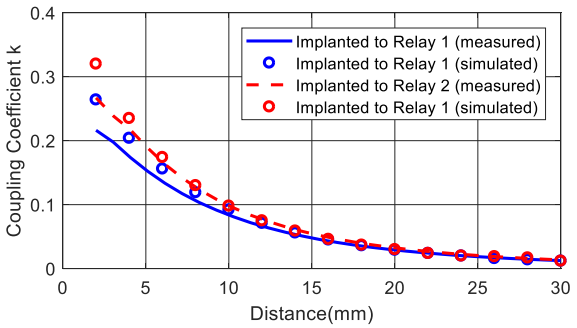

FIGURE 14. Simulated and measured coupling coefficients between the implanted antenna and different relay antennas described in Table 4.

the reader and the implanted antenna in the 2-coil system (see Fig.1b) is shown in Fig.12.

Fig.13 compares the coupling (k_{12}) between the relay and reader antennas in the 3-coil system. The coupling coefficient (k_{23}) between the relay and the implanted antennas in the 3-coil system is shown in Fig.14. Agreement between the measured and the simulated coupling coefficients was good. Some discrepancies were found when the coils were very close to each other. This is due to high sensitivity to the small misalignment and position errors for these distances. We conclude that close antennas with similar areas present strong coupling coefficients for small distances, while antennas with large areas present high coupling at long distances.

E. SYSTEM SIMULATIONS

To study the viability of using smartphones to power up implanted sensors, numerous simulations were carried out using the nonlinear model of the tag for both the 2-coil and 3-coil links. Fig.15 shows the Keysight ADS schematic used for the Harmonic Balance (HB) simulations with the 3-coil system (the schematic for the 2-coil system is identical but without the relay antenna). For the sake of clarity, the IC was included as a block (NFC_IC) and is described in section III.B. After HB simulation, the voltage for each harmonic and DC are available. The received power can therefore be obtained from a power probe at the input of the IC, while the AC voltage at the carrier and DC values

TABLE 5. Parameters used in the system simulations.

Parameter	Value
Source power (dBm)	20
Source resistance R_s (Ω)	4.86
Source voltage V_s (V)	0.98
Source capacitance C_1 (pF)	68.8
Reader antenna inductance L_1 (μH)	2
Reader quality factor Q_1	35
Relay inductance L_2 (μH)	0.7
Relay quality factor Q_2	70
Relay parasitic resistance R_{p2}(Ω)	700
Relay parasitic capacitance C_{p2} (pF)	0.07
Relay parasitic capacitance Cs_2 (pF)	0.4
Capacitance C_2 (pF)	196.7
Tag antenna inductance L_3 (μH)	0.7
Tag antenna quality factor Q_3	60
Tag parasitic resistance R_{p3} (Ω)	192
Tag parasitic capacitance C_{p3} (pF)	0.9
Relay parasitic capacitance Cs_3 (pF)	2.8
Tuning Capacitance C_{tun} (pF)	175.9

after the rectifier (V_{REC}) or regulator (V_{DD}) are computed by the simulator. Efficiency can be calculated from the ratio between the received and input power at the fundamental component (Probe 2 and Probe 1, respectively, in Fig.15). Input impedance can be obtained using a current probe at the input of the IC.

Using the values for inductance and quality factors obtained from simulations of the implanted and relay antennas, Table 5 shows the parameters taken into account for simulating efficiency and power transfer. The reader, which includes the matching network, is modeled using the equivalent circuit of Fig.3. It is assumed that the resistor R_Q in series with the reader antenna is added to lower the quality factor to 35, which is the overall quality factor of the reader needed for the transmission bandwidth. The source resistance R_s is the equivalent resistance, which is obtained from the quality factor ($R_s = 2\pi f_0/Q_1$). The value of the source amplitude is computed from the transmission power P_{Tx} ($V_s = (2P_{TX}R_s)^{1/2}$). C_1 is chosen to resonate at the operation frequency $f_0 = 13.56$ MHz ($C_1 = 1/(L_1 w_0^2)$). Capacitances C_2 and C_{tun} are adjusted to make the relay and tag antennas resonant at f_0.

Fig.16 shows simulations of the IC equivalent resistance and capacitance as a function of the coupling coefficient for the 2-coil system. Due to the nonlinear behavior of the NFC IC [38]–[40], R_{IC} resistance depends on the power received. The values of R_{IC} obtained are below the limit imposed by the maximum quality factor to ensure the bandwidth required for the backscattering communication given by (12). When the reader begins the interrogation, R_{IC} resistance is very high (several kΩ) but decreases when the NFC IC is woken and moves into operating mode. The value of R_{IC} resistance drops

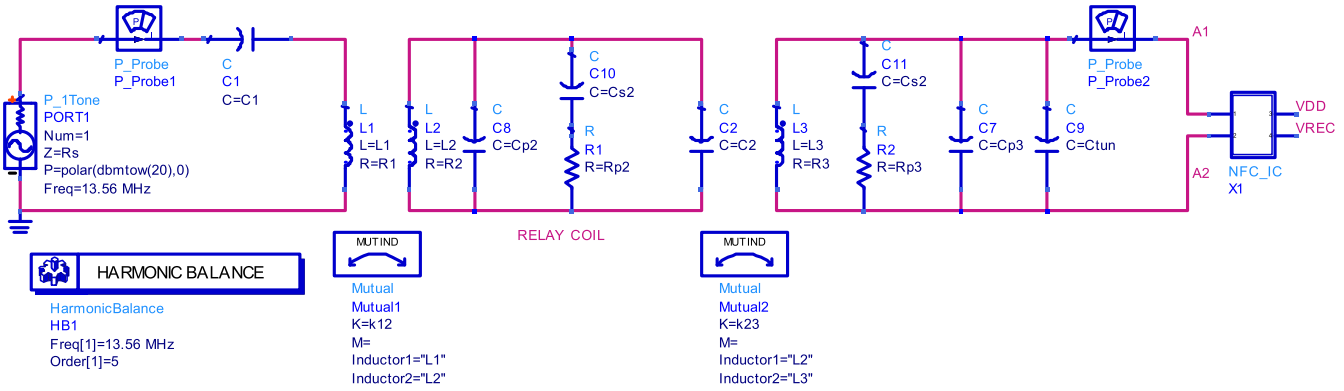

FIGURE 15. Schematic used for the Harmonic Balance simulation of the 3-coil system. The IC is represented as a block.

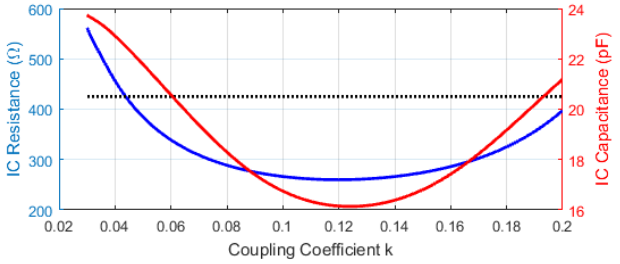

FIGURE 16. Simulated equivalent IC resistance (blue) and IC capacitance (red) as a function of the coupling coefficient in the 2-coil system. The threshold resistance at the threshold power is shown (dotted line).

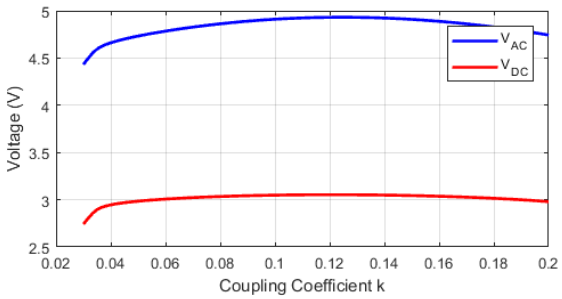

FIGURE 17. Simulated AC voltage at the receiver coil and DC voltage at the output of the shunt regulator as a function of the coupling coefficient in the 2-coil system.

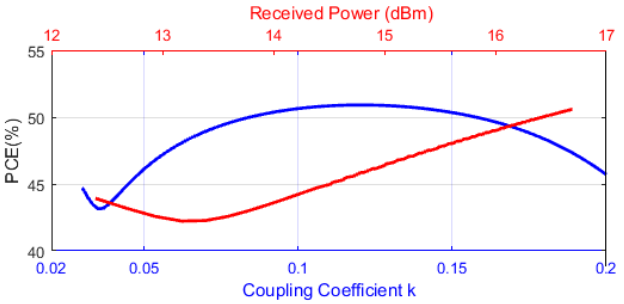

FIGURE 18. Simulated Power Conversion Efficiency as a function of the coupling coefficient in the 2-coil system (blue) and as a function of the received power (red).

when the AC voltage or power received at the antenna coil increases. For typical values of R_{IC} during the IC operating mode, the tag quality factor is limited by the load quality factor Q_L, which is considerably lower than the maximum value required. It is difficult to measure nonlinear IC impedance in the laboratory. This impedance is very mismatched compared to standard RF laboratory instruments (50 Ω). It is therefore difficult to excite the IC with enough power to activate it: since power is mostly reflected, high power levels are required to excite the IC. The excitation power level of a commercial VNA is often limited to 20 dBm (over 50 Ω). A modified VNA setup with an external amplifier and a reflectometer [38]–[40] to characterize the IC under similar power conditions to the actual operation with a reader is required. Experimental results obtained in the above studies for different ICs show the power dependence of the impedance obtained here in the simulations.

Fig.17 shows the AC voltage received at the (implanted) tag coil and the rectified voltage at the output of the shunt regulator as a function of the coupling coefficient between the antennas in the 2-coil system. The threshold power is the minimum power needed to obtain a stable DC voltage in the energy-harvesting output (e.g. 2.9V). In most commercial IC, the energy-harvesting output is disabled below this threshold. Therefore, under this level, the external microcontroller and sensors are not biased and a new sensor measurement cannot be taken. In commercial IC, this power level is higher than the minimum power required to read previously stored data in the NFC EEPROM. The RF limiter protection is designed to begin to actuate for AC levels in the antenna terminals above 4.8V. For higher levels, the AC voltage saturates, thus preventing damage to the transistors in the rectifier. Fig.18 shows the simulations of the Power Conversion Efficiency (PCE) of the rectifier as a function of the coupling coefficient and the received power. This efficiency is calculated by loading the output of the energy harvesting with a sink current of 3 mA, which simulates the current consumption of the sensors. Efficiencies of roughly 44% are achieved for the threshold power (14 dBm).

Fig.19 shows the power received and the efficiency as a function of the coupling for the 2-coil system in the air. Using

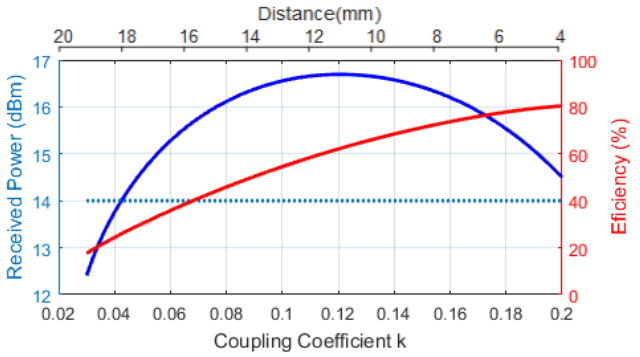

FIGURE 19. Simulated received power in dBm (blue) and efficiency (red) as a function of the coupling coefficient and the distance between the reader and the implanted antennas in the 2-coil system. The dotted line shows the power threshold.

data from Fig.12, the distance corresponding to the coupling between the reader antenna (reader 1) and the implanted antenna is added in the upper x-axis. For couplings above 0.04, the power received at the input of the tag is higher than the threshold power. The total distance between the reader and the implanted antenna is roughly 18 mm. A smartphone located at 5-10 mm can therefore provide energy to an implant at a depth of roughly 8-13 mm. For power levels above the threshold, the harvesting output is stable and can support the external DC load (assumed 3 mA). When the coupling coefficient is very high (>0.12), the power received decreases due to activation of the shunt limiter protection, thus increasing IC resistance. Due to the load modulation phenomenon, the mismatch at the input of the transmitter also increases for high coupling factors.

The simulations were repeated for the 3-coil system. In this case, there were two degrees of freedom: the coupling between the reader and the relay antennas (k_{12}), and the coupling between the relay and the implanted antennas (k_{23}). Fig.20 shows the received power and efficiency as a function of the coupling between the relay and the implanted antenna (k_{23}) for various couplings between the reader and the relay antennas (or equivalently, for various distances between the reader and the skin surface). IC impedance (Fig.21) presented the same nonlinear behavior as with 2 coils.

Fig.22 shows the received AC and rectified DC voltages as a function of the coupling between the relay and the implanted antennas (k_{23}) for two coupling values between the reader and relay antennas ($k_{12} = 0.05$ and $k_{12} = 0.1$). Coupling coefficients k_{23} above 0.05 and 0.08 are required for correct DC conversion, when $k_{12} = 0.05$ and 0.1, respectively. Fig.23 shows the received power and efficiency as a function of the coupling coefficient k_{23} or, equivalently, the depth of the implanted coil in the 3-coil system. Unlike with the 2-coil system, where efficiency is a monotonic function of the coupling, efficiency in the 3-coil system (Fig.23b) presents an optimum coupling k_{23} value that depends on k_{12} (11). The upper x-axis shows the distance corresponding to the reader 1 and relay 1 antennas obtained from

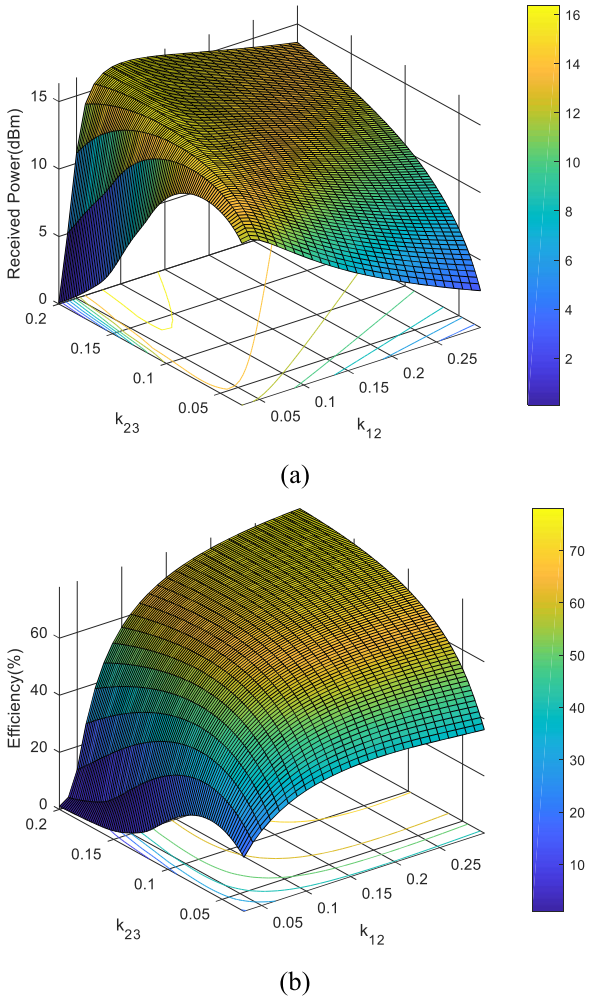

FIGURE 20. Simulated received power in dBm (a) and efficiency (b) as a function of the coupling coefficients in the 3-coil system.

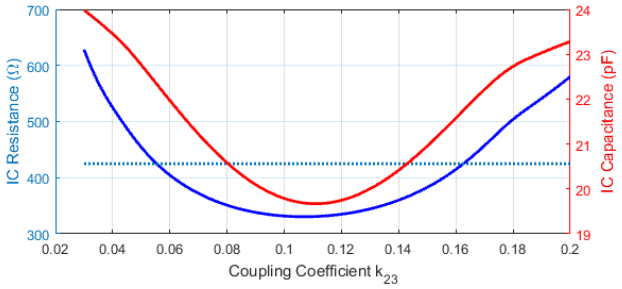

FIGURE 21. Simulated equivalent IC resistance (blue) and IC capacitance (red) as a function of the coupling coefficient in the 3-coil system ($k_{12} = 0.05$). The threshold resistance at the threshold power is shown (dotted line).

the graphs of the coupling coefficient as a function of the distance (Figs.12-14).

With the 3-coil system, for close coupling between the reader and relay (distance in the order of 1 cm in Fig.23), the maximum depth of the implant can increase to 18-21 mm (Fig.23). Although this improvement does not seem great,

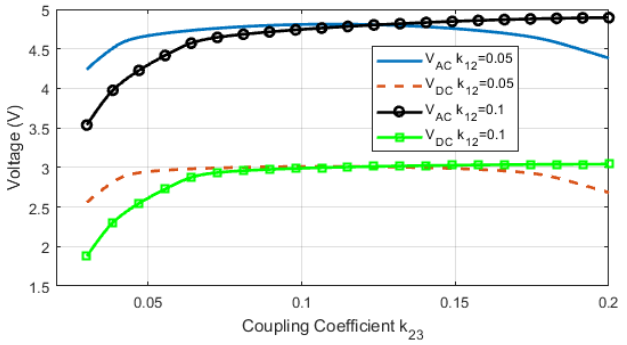

FIGURE 22. Simulated AC voltage at the receiver coil and DC voltage at the output of the shunt regulator as a function of the coupling coefficient between the implanted and relay antennas in the 3-coil system.

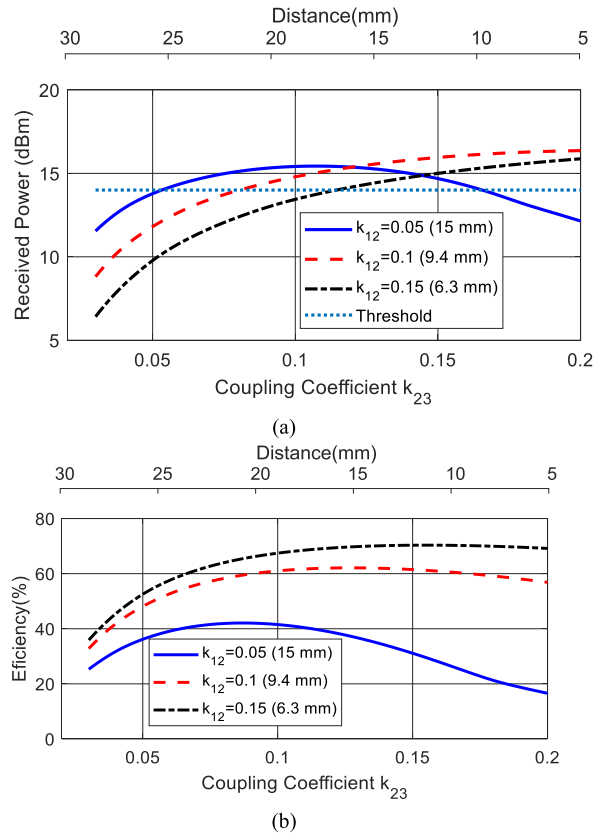

FIGURE 23. Simulated received power in dBm (a) and efficiency (b) as a function of the coupling coefficient and the distance between the relay and implanted antennas in the 3-coil system. Various coupling coefficients between the reader and relay antennas are considered (distance is indicated in parenthesis).

the second system is more tolerant of misalignment between antennas. The relay and implanted antennas are assumed to be center-aligned. The relay antenna on the skin can easily be used to localize the tag, and small misalignments in the horizontal plane can be tolerated because the coupling between the reader and the relay is strong for typical distances (3-10 mm). In the 2-coil system it is more difficult to align the antennas due to the lack of any reference to indicate the implant's exact position. Horizontal misalignments for distances between the smartphone and the implant of over 10 mm can therefore lead to a rapid decrease in the coupling coefficient [72], especially if the reader uses small area antennas (which are the most common in modern mobiles with metallic cases). The above practical consideration enables the 3-coil system to detect implanted NFC tags up to 16 mm deep inside the body with a distance between mobile and skin of 5-10 mm.

IV. EXPERIMENTAL RESULTS

We conducted numerous experiments to check the two systems and compare them to the simulations. We also performed several measurements with an implanted tag. A phantom comprising slices of pork tenderloin was used. The tag was covered with a plastic bag (PTE) to emulate the protection layer in a real implant, assuming that the dielectric properties are similar to those of silicone. The thickness of the bag (made of PET, $\varepsilon_r \approx 2.5$) was 0.1 mm. This may therefore be considered the worst case. Relay antenna 1, as described in Table 4 (4 turns and an area of 25 mm $\times$ 25 mm), was used in the experiments. However, to perform the measurement closer to a real NFC patch attached to the skin, the relay antenna was designed and manufactured in flexible Ultralam 3000 (Rogers Inc.) substrate ($\varepsilon_r = 3.14$, thickness 100 μm). This may be considered the worst case because the coil was very close to the skin. A parallel capacitor was used to adjust the resonance frequency to 13.56 MHz and avoid the detuning effect due to the high permittivity of the phantom. No significant changes were observed in the read range compared to a rigid relay antenna manufactured on FR4 with a thickness of 0.8 mm and tuned at 13.56 MHz.

A. EFFICIENCY MEASUREMENTS

S parameter measurements were performed using the vector network analyzer (VNA) for the 2-coil and 3-coil systems. From these measurements, the efficiency and received power at the input of the tag were computed. The laboratory instruments presented a reference impedance of 50 Ω, which is different from the IC input impedance and the source impedance of the reader. To refer to these impedances, the measurements were loaded in the Keysight ADS simulator using a two-port S parameter data item and its block was loaded with the tuning capacitors and the desired loads in accordance with the schemes in Fig.1. In view of the previous results and the impedance simulations, $R_{IC} = 525\ \Omega$ was chosen. The source resistance was set to achieve a maximum Q factor of 35. A series capacitor (220 pF) at the input and a parallel capacitor (190 pF) at the output were included in order to tune the system at the operation frequency of 13.56 MHz. These values did not change in any measurement. The 15×15 mm implanted coil with 6 turns made with a 0.8 mm thick FR4 double-sided PCB was used. Coil reader 1 described in Table 4 (25×25 mm with 4 turns on FR4 substrate) was used to simulate the reader. The implanted coil was embedded in a piece of pork sirloin, which was used as a phantom to simulate the body. A linear actuator controlled the distance

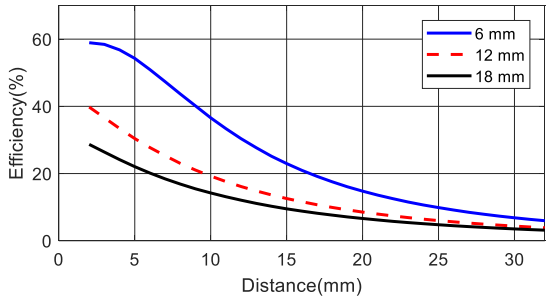

FIGURE 24. Measured efficiency as a function of the distance between the antenna reader and the skin surface for several depths of the implanted antenna for the 2-coil system.

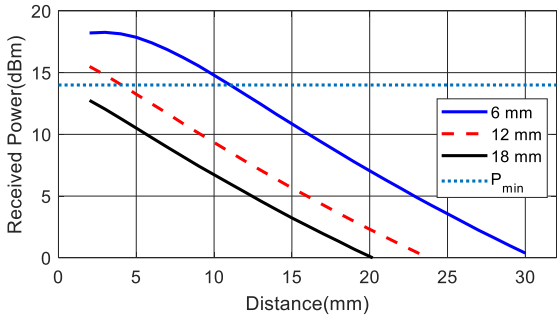

FIGURE 25. Measured received power as a function of the distance between the antenna reader and the skin surface for several depths of the implanted antenna for the 2-coil system.

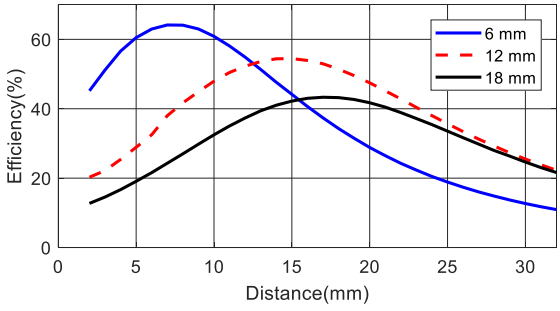

FIGURE 26. Measured efficiency as a function of the distance between the antenna reader and the skin surface for several depths of the implanted antenna for the 3-coil system.

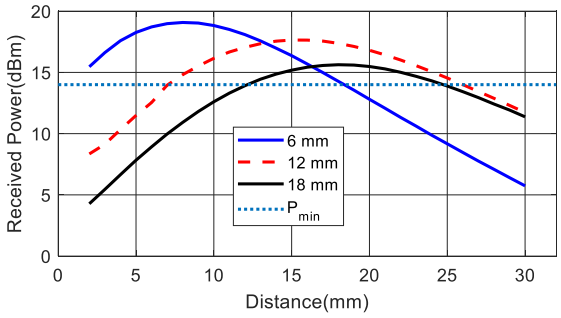

FIGURE 27. Measured received power as a function of the distance between the antenna reader and the skin surface for several depths of the implanted antenna for the 3-coil system.

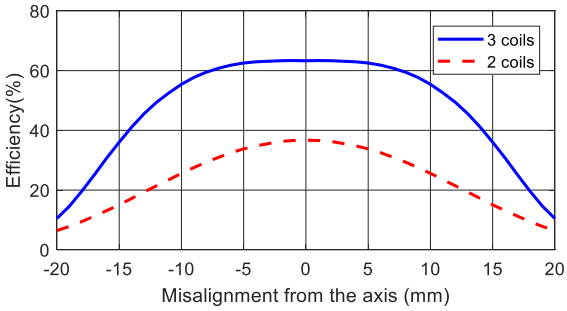

FIGURE 28. Measured efficiency as a function of the misalignment distance from the axis for the 2-coil and 3-coil systems. The depth of the implanted antenna was 6 mm and the distance between the reader antenna and the skin surface was 10 mm.

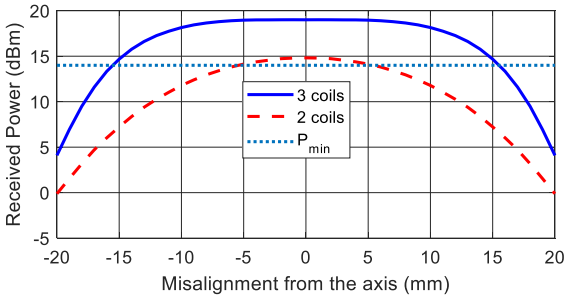

FIGURE 29. Measured received power as a function of the misalignment distance from the axis for the 2-coil and 3-coil systems. The depth of the implanted antenna was 6 mm and the distance between the reader antenna and the skin surface was 10 mm.

with a stepper motor. Fig.24-25 and Fig.26-27 show the measured efficiency and received power as functions of the distance between the surface of the meat and the reader coil for the 2-coil and 3-coil systems, respectively. In these graphs, various depths of the implant between 6 mm and 18 mm were considered. The reverse side was covered by 2 cm of meat. To investigate the effect of misalignment between coils, we took several measurements of efficiency and received power. The reader antenna (reader 1) was misaligned from the axis using the linear actuator. The distance between the reader antenna and the surface of the phantom was set at 1 cm. The depth of the implanted antenna was 6 mm.

Fig.28-29 compare the efficiency and received power for the 2-coil and 3-coil systems. Whereas the efficiency and the power level remained almost constant for the ±12.5 mm range, which corresponds to the overlap between the reader and relay antennas, there was a rapid fall for the 2-coil system. These results show that the 3-coil system is more robust than the 2-coil system.

B. WPT WITH SMARTPHONE

To test the system with commercial smartphones as an NFC reader and commercial NFC IC, we designed another experimental setup. The main problem here was that the antenna in the reader was not accessible. Moreover, the previous measurements did not take into account the nonlinear behavior of the tag or the effects of the proximity of the mobile's metal case, which can detune the coils [27]. To solve these

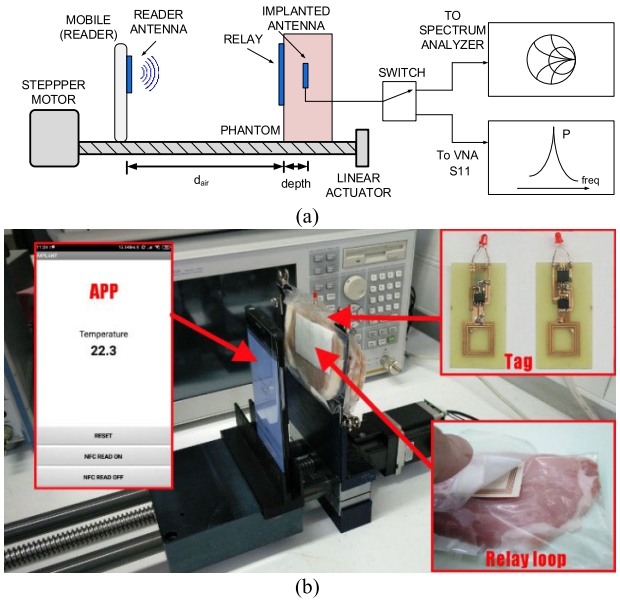

FIGURE 30. **(a) Setup used to measure the average magnetic field, (b) photograph of the setup for read range measurements, including a screenshot of the mobile application.**

problems, measurements of the average magnetic field (H_{av}) received by the tag as a function of the distance were used to compare the performance of the readers and tags. H_{av} measurements are often used for the certification of devices in NFC forum standards.

An experimental setup was designed to measure the average magnetic field and read range measurements. Fig.30a shows a schema of this setup, while Fig.30b shows a photograph of the setup used for the read-range measurement. A mobile phone was used as a reader to interrogate the tag. An application was designed to enable interrogation during the measurements and to read the sensor data stored in the NFC message using the NFC Data Exchange Format (NDEF) (Fig.30b). The same loop antenna as was used in the tag was connected to a microwave switch (Minicircuits model MSP2T-18) to select the spectrum analyzer (SA, Rohde & Schwarz model FSP3) or vector network analyzer (VNA, Agilent model E5062A) to perform measurements at each distance. The VNA was calibrated to the input of the antenna. When the switch was in the SA position, the power received at the carrier frequency was measured using the maximum hold trace. In the VNA position, the reflection coefficient of the antenna was measured to obtain its impedance from the S_{11} parameter. These measurements can be used to obtain the average magnetic field from the antenna factor (AF) obtained from the loop impedance [27], [73]:

$$H_{av}(A_{RMS}/m) = V_{RMS} \cdot |AF| \tag{19}$$

$$AF = \frac{Z_0 + Z_{in}}{j2\pi f \mu_0 Z_0 A \cdot N} \tag{20}$$

where Z_0 is the reference impedance (50 Ω) and Z_{in} is the input impedance of the antenna measured with the VNA. The root mean square voltage (V_{RMS}) is obtained from the power measured with the spectrum analyzer.

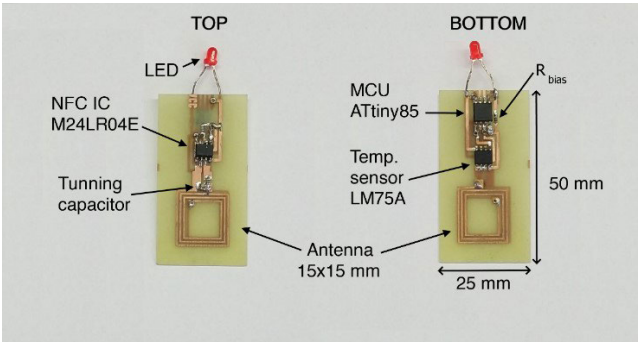

FIGURE 31. **Photograph of the tag manufactured for measurements: top view (left) and bottom view (right).**

To obtain a repeatable measurement, the distance between the reader and the coils was controlled by a linear actuator with a stepper motor. The mobile and tag were supported by pedestals designed with a 3D printer. After this measurement, the tag antenna coil was replaced by a tag with the harvesting DC output connected to an oscilloscope. The minimum magnetic field was determined when the tag was unable to activate the harvesting output, so the microcontroller and sensors were not biased. The tag used in the experiments contained the 15×15 mm implanted coil with 6 turns made with a 0.8 mm thick FR4 double-sided PCB (see Fig.31). The tag used was the ST M24LR04E NFC IC with energy-harvesting capabilities and was connected to an Atmel ATtiny85 microcontroller with a clock frequency of 1 MHz, which was connected to the sensors. The microcontroller was responsible for reading the sensor data and saving them in the NDEF message in the internal EEPROM of the NFC IC by I2C bus. These data could be read by the mobile. It is important to note that the read range is limited by the energy harvesting required to power up the sensors and the microcontroller. The distance at which the data previously stored in the memory of the NFC IC can be downloaded by RF communication (downlink) is greater than in the downlink because of the high sensitivity of the NFC transceivers. As proof of this concept, a temperature sensor (Texas Instruments LM75A) was integrated. The temperature was read by the microcontroller using the I2C bus. The data were stored in the NDEF message read by the mobile. A red LED was connected to the energy harvesting voltage output to quickly monitor the energy harvesting. The current through the LED was limited with a series-connected bias resistor R_{bias} (see Fig.31). The value of the bias resistor R_{bias} was adjusted to simulate maximum power consumption. The tag drew a total of 3 mA at 3V in its normal operating state. The two systems with 2 and 3 coils were measured. The NFC IC was configured to the highest energy-harvesting mode, which, in the worst-case scenario, would require a higher magnetic field. Since biological materials are not magnetic, we expected their effect to be small except, as explained earlier, in the detuning of the antennas.

Several tests were therefore first performed in the air. Fig.32 shows the measurement of the 2-coil system with no

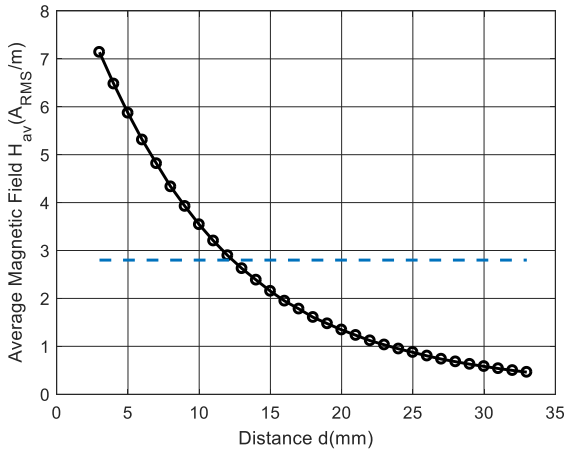

FIGURE 32. Average magnetic field, measured as a function of the tag-to-reader distance in the air for the 2-coil system. Threshold H_{min} is shown as a dashed line.

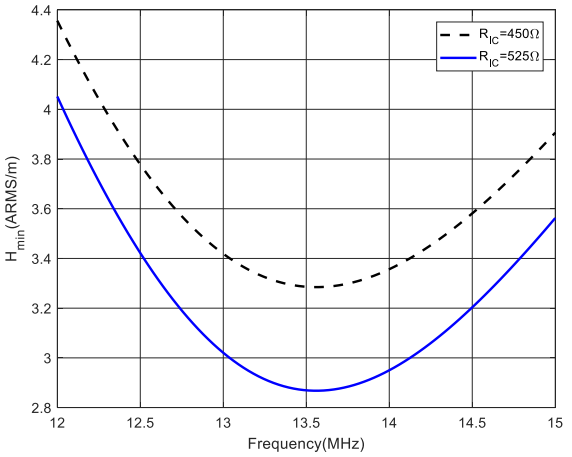

FIGURE 34. Simulated threshold magnetic field H_{min} as a function of the frequency.

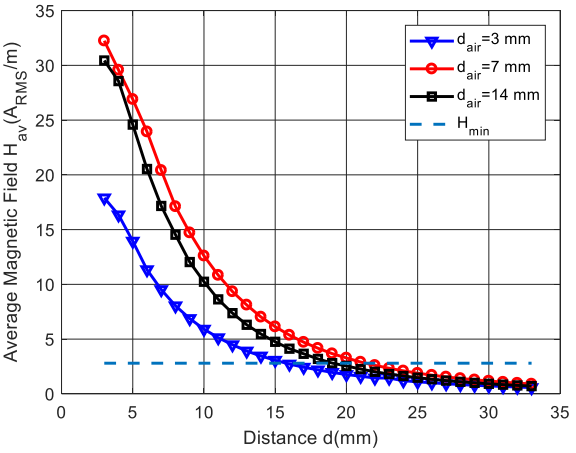

FIGURE 33. Average magnetic field measured as a function of the distance between the tag and the relay antenna for several distances to the reader in the air (d_{air}) for the 3-coil system.

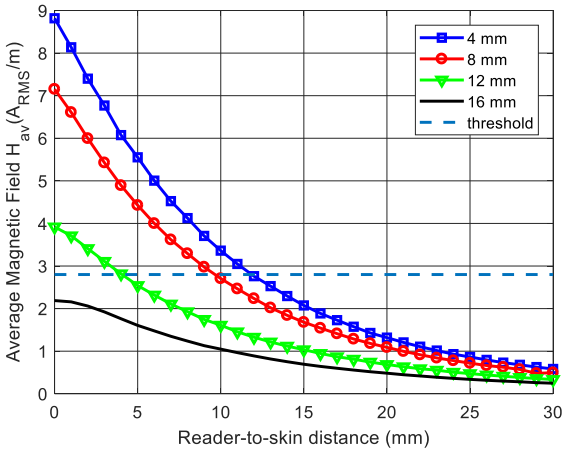

FIGURE 35. Measured average magnetic field as a function of the reader-to-skin distance (d_{air}) for several depths of the implanted tag in the phantom for the 2-coil system. Threshold H_{min} is shown as a dashed line.

material between the tag and the reader (in air). Fig.33 plots the measured average magnetic field as a function of the reader-to-tag distance for a different distance between the relay antenna and the coil tag antenna. Our results show that the minimum threshold magnetic field was around 2.8 A_{RMS}/m in both cases, which corresponds to a read range of roughly 12 mm for the 2-coil system and read ranges of between 15-20 mm for the 3-coil system.

Alternatively, the value of the threshold average magnetic field H_{min} can be found from the analytical expression given in [29]:

$$H_{min} \approx \frac{\sqrt{\left[1-\left(\frac{f}{f_r}\right)^2\right]^2+\frac{1}{Q_{2L}^2}}}{2\pi f \mu_0 A \cdot N} \cdot U_{min} \qquad (21)$$

where f_r is the resonance frequency of the tag, A is the loop area, N is the number of loops andU_{min} is the minimum voltage required for the tag operation, which depends on the chip IC. Fig.34 shows the simulated H_{min} obtained from (21) by considering $R_{IC} = 525\ \Omega$, tag inductance $L = 0.7\ \mu$H, $Q = 70$, $A = 15{\times}15$ mm^2, and $N = 6$. $U_{min} = 4.8$V was obtained by measuring with a low capacitance probe and the oscilloscope at the read range distance. H_{min} may be considered a figure of merit of the tag because it depends only on the tag parameters (the IC and the receiver antenna). It can, therefore, be used to evaluate the tag performance regardless of the reader used to generate the field. A good agreement was achieved between the experimental characterization of the H_{min} and the analytical model. From these results, the threshold or minimum power that activates the energy-harvesting output was 13.2 dBm (which is very close to the 14 dBm considered in the simulation in section E). The estimated power conversion with a load of 3 mA and the static DC current consumption shown in the datasheet (around 400 μA) gave a PCE of 42.82 %, which is close to the figure obtained with the rectifier simulated in section E.

Fig.35 shows the measured average magnetic field as a function of the reader-to-skin distance (d_{air}) for several

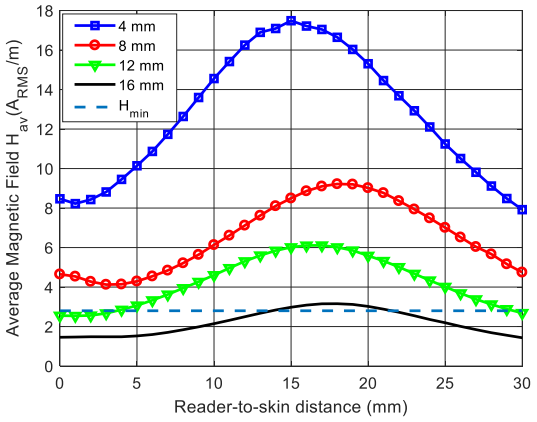

FIGURE 36. Measured average magnetic field as a function of the reader-to-skin distance (d_{air}) for several depths of the implanted tag in the phantom for the 3-coil system. Threshold H_{min} is shown as a dashed line.

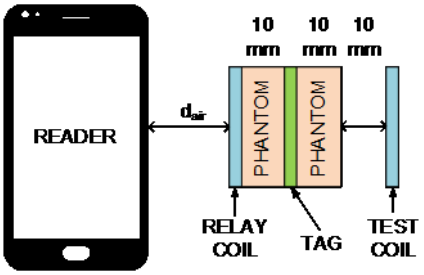

FIGURE 37. Setup for backscattering measurements consisting of the reader, the relay coil (only in the 3-coil system), the implanted tag surrounded by the phantom, and a test coil connected to the oscilloscope and spectrum analyzer.

depths of the implanted tag for the 2-coil system. Finally, Fig.36 shows the same measurement as Fig.35 for the 3-coil system.

We have shown that implanted distances of up to 16 mm can be reached with the 3-coil system. However, detuning of the relay antenna is observed due to the proximity of the metal in the mobile. The peak of the magnetic field is therefore obtained for distances between the reader and the skin of around 15 mm. The position of this peak can be tuned by changing the resonance frequency of the relay antenna the tuning capacitor. Fig.36 shows that the 3-coil system is more robust than the 2-coil system. In all measurements, a commercial mobile (Xiaomi Note 2) was used as the reader. The reader antenna in this mobile is around the camera and the size of the antenna is roughly 25 mm × 25 mm (like reader antenna 1-2 in Table 4).

C. BACKSCATTERING MEASUREMENTS

When the tag receives enough power to wake up the NFC IC, the tag answers by modulating a subcarrier. Modern receivers integrated into NFC readers are highly sensitive (for example, 0.5 mV or −79 dBm for ST25R3911B). It is important to note, therefore, that the distance is limited by the uplink (reader to tag) since the backscattering is often higher than

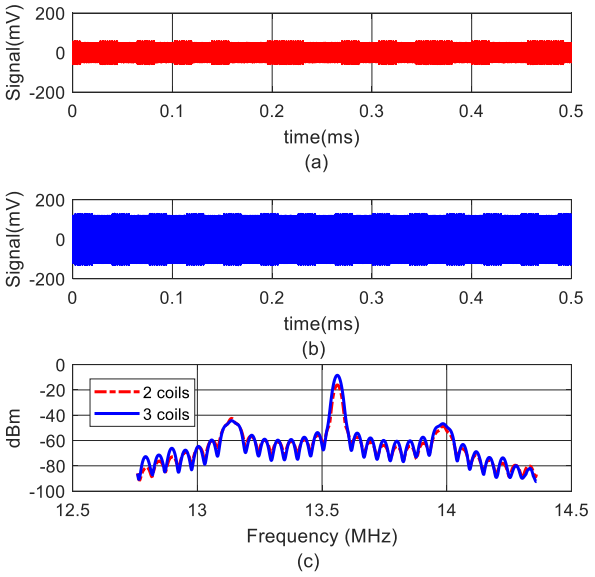

FIGURE 38. Measured backscattering signal using a test coil 2 cm from the implant (10 mm deep) for (a) the 2-coil system and (b) the 3-coil system. (c) Spectrum obtained from Fourier Transform of time-domain signal for the two systems.

the receiver's sensitivity. Commercial NFC IC with energy harvesting (such as the ST M24LR04E) enables the energy-harvesting DC output used to feed the sensors and microcontroller when the received power is high enough. Otherwise, while the energy is higher than the power needed to wake up the IC, the NFC IC works as a conventional NFC IC without energy harvesting and is able to respond by load modulation. In this case, however, a previously saved measurement in the NFC memory is transmitted. Consequently, the read range without activation of energy harvesting is higher than when EH output is enabled.

To show this effect, a test coil located 20 mm behind the implant was connected to an oscilloscope (R&S RTO2024 with 50 Ω input impedance). The mobile was located 20 mm in front of the implant, which was placed inside a phantom at a depth of 10 mm (Fig.37). Fig.38 shows the waveform corresponding to the backscattering response to a query command from the mobile. The two cases (2 and 3 coils) are shown in Fig.38a and 38b, respectively. Fig.38c represents the magnitude of the spectrum computed by the oscilloscope math function. We can see that the level at the subcarrier (offset of ± 424 kHz from the 13.56 MHz carrier for tags based on ISO15693 standard) was approximately the same for both systems (roughly -43 dBm, which is higher than the reader sensitivity). However, at a distance of 20 mm in the 3-coil system, the harvesting was enabled and a new measurement was performed, whereas for the 2-coil system the magnetic field received was lower than the energy harvesting threshold. As a result, the interrogator obtained the last measurement stored in the tag memory rather than a new one.

Figure 39 shows measurements of the backscattering power with a spectrum analyzer connected to the test coil as a

TABLE 6. Comparison table.

Item	[75]	[76]	[77]	[5]	This work
Carrier Frequency (MHz)	13.56	10	13.56	13.56	13.56
Power (mW)	11.2	10	100***	6**	10-19.8
Link Efficiency(%)	6.9	NA	26-74 (sim)	NA	45-60
Range (mm)	10	8	3-4 (phantom) 15 (air)	Near skin 25 (air)	16 (phantom)+30 (air)*
Medium	Air	Rat	phantom	In-vivo	phantom
Inductive link	2 coils	2 coils	2 coils	2 coils	2/3 coils
Tx Coil diameter (mm)	20	30	25	NA	20-40
Rx Coil diameter (mm)	10	20	16	3.3 (ferrite)	15
Data Rate	600 bps	2Mbps (Tx)/100kbps(Rx)	1.35 Mbps	NA	26.4-53 kbps
Modulation	LSK	LSK, ASK	PPSK,OOK	ASK	ASK, FSK
Technology	COST	ASIC	ASIC	ASIC	Commercial IC
Microcontroller	TI MSP430	-	-	-	ATtiny85
Reader	TI TRF7960	Custom	Custom	Custom	Smartphone
Standard	No	No	No	ISO15693	ISO15693
Application	Generic	Brain stimulation	Vestibular prosthesis	Glucose sensor	Generic

*16 within the phantom and 30 in the air for the 3-coil system
**Estimated from DC power consumption
***Maximum power delivered by the IC to the load

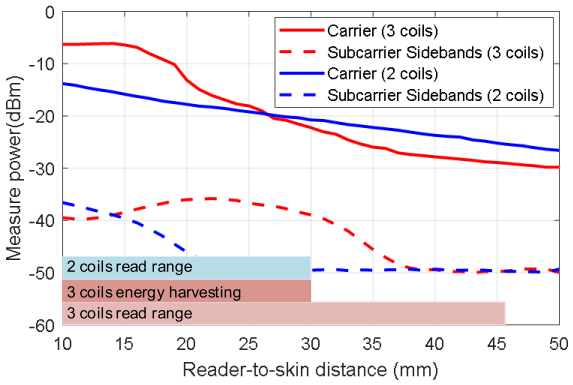

FIGURE 39. Measured backscattering signal using a test coil located 2 cm behind the implanted tag in the phantom as a function of reader-to-skin distance (d_{air}). Solid line: measured power at the carrier frequency (13.56 MHz); dashed line: average sideband power.

function of the reader-to-skin distance. The power measured at the carrier frequency (13.56 MHz) and the average power level at the subcarrier sidebands (at ± 424 KHz from the 13.56 MHz carrier) are shown for the two systems. The test coil was located 2 cm behind the phantom and the depth of the implanted tag in the phantom was 10 mm (see Fig.37). Under this condition, the 2-coil system was unable to activate the energy harvesting output but was able to read the tag up to approximately 3 cm. The 3-coil system, on the other hand, was able to activate energy harvesting up to 3 cm and to read the tag up to 4.6 cm. The nonlinear behavior of the backscattered power at the tag can be seen in this figure. When the received power was high, the internal input limiter was activated and the level at the subcarrier remained almost constant, irrespective of the distance. However, when the reader-to-tag distance increased, both the received level and backscattered level decreased. If the tag did not receive enough power to be woken up, the measured level at the subcarrier was the noise floor.

V. COMPARISON WITH THE STATE-OF-THE-ART

Although lower carrier frequencies such as 135 kHz can provide higher power and reach greater depths, the data rate is often very low and insufficient for several IMD applications [74]. For this reason, the band between 1-20 MHz is preferred for WPT and bidirectional telemetry data communication. A comparison of the main features of the proposed system with other works [5], [75]–[77] at the carrier frequency of 13.56 MHz (or close to it) is shown in Table 6. This comparison is limited to a single-receiver coil. Higher data rate transfers are demonstrated in [78], which used dual receiver coils. Reference [75] proposed a system built with Commercial Off-The-Shelf (COTS) components. The tag consists of a full-wave rectifier based on diodes and a MSP430 microcontroller that can modulate data at 600 bps using a load modulation key (LSK). The power delivered in the systems reported in Table 6 is roughly 10 mW, except in [77], which reports a power of up to 100 mW but does not provide data on the experimental setup or conditions used. Most of the systems reported are based on application-specific integrated circuits (ASICs) designed for the application. These are not standardized and require custom readers. In [5], an ASIC compatible with ISO 15693 is reported for in-vivo glucose

monitoring. The WPT is used to feed a LED, while the photodiodes for detecting the fluorescent emission are used for long-term implantable glucose sensing. A wearable transmitter periodically interrogates the tag with a ferrite antenna located under the skin. References [5] and [75]–[77] use a 2-coil system. Read ranges of up to 25 mm are reported in air and up to 8 mm in the body. In comparison with these references, the 3-coil solution proposed in this paper increases the read range to 16 mm when implanted plus 3 cm in the air (between the mobile and the skin) using, moreover, a standard smartphone and commercial NFC IC. Also, by integrating a microcontroller and the NFC IC's internal memory, further tools are added to the interface of the advanced sensors. In the proof-of-concept presented, a LED is biased and a I2C-connected temperature sensor is read. The data rate in the IC based on ISO15693 is up to 26.4 kbps. However, some IC (e.g. ST M24LR04E) based on FSK modulation with two subcarriers have a high rate mode that can reach up to 53 kbps. Higher data rates of up to 848 kbps can be achieved by using NFC IC based on ISO 14443 (see the table provided in [27] of commercial IC with EH). Higher data rates have also been achieved [76], [77] using custom ASICs.

A passive booster for improving the read range of small NFC tags designed for metal mounted has been proposed in [79]. Unlike this work, the relay loop is installed in the mobile phone casing, assuming that the NFC antenna is installed on the battery with a plastic case. The booster has two coils, one used for coupling to the mobile and the other one, with smaller size (similar to the tag), to improve the coupling with the miniature tag mounted on the metal. Due to its small size, careful alignment is required between the booster and the tag. The read range is limited by the diameter of the tag to few millimeters.

VI. CONCLUSION

This paper has analyzed the reading of batteryless NFC tags for implants using commercial mobiles. Using standardized NFC readers and devices rather than custom-designed WPT systems presents a number of challenges such as the power and the system's overall quality factor and detuning effects. In this paper, two WPT systems, i.e. a 2-coil system and a 3-coil system, were studied theoretically and experimentally. The latter was implemented using a relay antenna placed on top of the skin. This makes it possible to reduce the effects of the low coupling coefficient between the reader and the tag antennas, which can be of different sizes and enables the magnetic field received at the tag to increase. The result is an increase in the reliability of the link and a greater depth for the implant. This is important when the implant is covered by clothes and it is difficult to see its exact position, thus increasing the possibility of misalignment. Our experimental results show that when a standard 2-coil system is used, a maximum depth of 12 mm can be achieved with the mobile close to the skin, whereas with the 3-coil system and the mobile placed at a distance of 1-2 cm from the skin, depths of up to 16 mm can be achieved. We have found that the read range is much higher without energy harvesting than with it (approximately 3 cm for the 2-coil system and 4 cm for the 3-coil system). The maximum distances for activating the harvesting mode of the NFC IC and feeding the sensors are similar when the implant is considered inside the phantom or in the air. This is because the body is non-magnetic and so barely attenuates the magnetic field at the operating frequency. However, both the implanted and the relay antennas need to be tuned for each case. The effect of detuning was studied using electromagnetic simulations, while an improved model was proposed for modeling the quality factor of the antennas. The detuning effects due to high permittivity on the loop antennas were avoided by installing a low permittivity spacer in the order of 0.5 to 1 mm. The relay antenna can then be placed on top of the skin using adhesive patches. The use of low permittivity coating (e.g. a biocompatible material such as silicone) reduced the degradation in the quality factor of the coils as well as the sensitivity in connection with the variation in tissue dielectric properties.

REFERENCES

[1] H. Dinis and P. M. Mendes, "Recent advances on implantable wireless sensor networks," in *Wireless Sensor Networks—Insights and Innovations*, P. Sallis, Ed. Rijeka. Croatia: InTech, Oct. 2017. [Online]. Available: https://www.intechopen.com/books/wireless-sensor-networks-insights-and-innovations/recent-advances-on-implantable-wireless-sensor-networks

[2] M. Schormans, V. Valente, and A. Demosthenous, "Practical inductive link design for biomedical wireless power transfer: A tutorial," *IEEE Trans. Biomed. Circuits Syst.*, vol. 12, no. 5, pp. 1112–1130, Oct. 2018.

[3] B. Mckean and D. Gough, "A telemetry-instrumentation system for chronically implanted glucose and oxygen sensors," *IEEE Trans. Biomed. Eng.*, vol. BME-35, no. 7, pp. 526–532, Jul. 1988.

[4] N. Anabtawi, S. Freeman, and R. Ferzli, "A fully implantable, NFC enabled, continuous interstitial glucose monitor," in *Proc. IEEE-EMBS Int. Conf. Biomed. Health Informat. (BHI)*, Las Vegas, NV, USA, Feb. 2016, pp. 612–615.

[5] A. Dehennis, S. Getzlaff, D. Grice, and M. Mailand, "An NFC–enabled CMOS IC for a wireless fully implantable glucose sensor," *IEEE J. Biomed. Health Inform.*, vol. 20, no. 1, pp. 18–28, Jan. 2016.

[6] M. C. Frost and M. E. Meyerhoff, "Implantable chemical sensors for real-time clinical monitoring: Progress and challenges," *Current Opinion Chem. Biol.*, vol. 6, no. 5, pp. 633–641, Oct. 2002.

[7] R. Farra, N. F. Sheppard, L. Mccabe, R. M. Neer, J. M. Anderson, J. T. Santini, M. J. Cima, and R. Langer, "First-in-human testing of a wirelessly controlled drug delivery microchip," *Sci. Transl. Med.*, vol. 4, no. 122, Feb. 2012, Art. no. 122ra21.

[8] G. Yilmaz and C. Dehollain, "Single frequency wireless power transfer and full-duplex communication system for intracranial epilepsy monitoring," *Microelectron. J.*, vol. 45, no. 12, pp. 1595–1602, Dec. 2014.

[9] Z. Yang, Q. Zhao, E. Keefer, and W. Liu, "Noise characterization, modeling, and reduction for *in vivo* neural recording," in *Proc. Adv. Neural Inf. Process. Syst.*, vol. 22, 2009, pp. 2160–2168.

[10] K. Bazaka and M. Jacob, "Implantable devices: Issues and challenges," *Electronics*, vol. 2, no. 4, pp. 1–34, Dec. 2012.

[11] J.-C. Chiou, S.-H. Hsu, Y.-T. Liao, Y.-C. Huang, G.-T. Yeh, C.-K. Kuei, and K.-S. Dai, "Toward a wirelessly powered on–lens intraocular pressure monitoring system," *IEEE J. Biomed. Health Inform.*, vol. 20, no. 5, pp. 1216–1224, Sep. 2016.

[12] M. H. Ghaed, G. Chen, R.-U. Haque, M. Wieckowski, Y. Kim, G. Kim, Y. Lee, I. Lee, D. Fick, D. Kim, M. Seok, K. D. Wise, D. Blaauw, and D. Sylvester, "Circuits for a cubic–millimeter energy–autonomous wireless intraocular pressure monitor," *IEEE Trans. Circuits Syst. I, Reg. Papers*, vol. 60, no. 12, pp. 3152–3162, Dec. 2013.

[13] G. Chitnis, T. Maleki, B. Samuels, L. B. Cantor, and B. Ziaie, "A minimally invasive implantable wireless pressure sensor for continuous IOP monitoring," *IEEE Trans. Biomed. Eng.*, vol. 60, no. 1, pp. 250–256, Jan. 2013.

[14] P. D. Costa, P. P. Rodrigues, A. H. Reis, and A. Costa-Pereira, "A review on remote monitoring technology applied to implantable electronic cardiovascular devices," *Telemedicine e-Health*, vol. 16, no. 10, pp. 1042–1050, Dec. 2010.
[15] M. A. Hannan, S. Mutashar, S. A. Samad, and A. Hussain, "Energy harvesting for the implantable biomedical devices: Issues and challenges," *Biomed. Eng. OnLine*, vol. 13, no. 1, p. 79, 2014.
[16] D. Seo, R. M. Neely, K. Shen, U. Singhal, E. Alon, J. M. Rabaey, J. M. Carmena, and M. M. Maharbiz, "Wireless recording in the peripheral nervous system with ultrasonic neural dust," *Neuron*, vol. 91, no. 3, pp. 529–539, Aug. 2016.
[17] G. E. Santagati and T. Melodia, "Experimental evaluation of impulsive ultrasonic intra–body communications for implantable biomedical devices," *IEEE Trans. Mobile Comput.*, vol. 16, no. 2, pp. 367–380, Feb. 2017.
[18] K. Goto, T. Nakagawa, O. Nakamura, and S. Kawata, "An implantable power supply with an optically rechargeable lithium battery," *IEEE Trans. Biomed. Eng.*, vol. 48, no. 7, pp. 830–833, Jul. 2001.
[19] W. Phillips, B. Towe, and P. Larson, "An ultrasonically-driven piezoelectric neural stimulator," in *Proc. 25th Annu. Int. Conf. Eng. Med. Biol. Soc.*, Cancun, Mexico, Jun. 2004, pp. 1983–1986.
[20] M. Kiani, U.-M. Jow, and M. Ghovanloo, "Design and optimization of a 3-coil inductive link for efficient wireless power transmission," *IEEE Trans. Biomed. Circuits Syst.*, vol. 5, no. 6, pp. 579–591, Dec. 2011.
[21] J. I. Agbinya, *Wireless Power Transfer*, 2nd ed, Delft, The Netherlands: River Publishers, 2016.
[22] G. Yilmaz, C. Dehollain, *Wireless Power Transfer and Data Communication for Neural Implants*. Cham, Switzerland: Springer, 2017.
[23] K. Finkenzeller, D. Müller, *RFID Handbook: Fundamentals and Applications in Contactless Smart Cards, Radio Frequency Identification and Near-Field Communication*, 3rd ed. New York, NY, USA: Wiley, 2010.
[24] M. Alibakhshi-Kenari, R. Ali Sadeghzadeh, M. Naser-Moghadasi, E. Limiti, and B. S. Virdee, "Dual-band RFID tag antenna based on the Hilbert-curve fractal for HF and UHF applications," *IET Circuits, Devices Syst.*, vol. 10, no. 2, pp. 140–146, Mar. 2016.
[25] D. Paret, *Design Constraints for NFC Devices*, 1st ed. Hoboken, NJ, USA: Wiley, 2016.
[26] B. Ozdenizci, V. Coskun, and K. Ok, "NFC internal: An indoor navigation system," *Sensors*, vol. 15, no. 4, pp. 7571–7595, Mar. 2015.
[27] A. Lazaro, R. Villarino, and D. Girbau, "A survey of NFC sensors based on energy harvesting for IoT applications," *Sensors*, vol. 18, no. 11, p. 3746, Nov. 2018.
[28] M. Boada, A. Lazaro, R. Villarino, and D. Girbau, "Battery–less soil moisture measurement system based on a NFC device with energy harvesting capability," *IEEE Sensors J.*, vol. 18, no. 13, pp. 5541–5549, Jul. 2018.
[29] M. Boada, A. Lazaro, R. Villarino, and D. Girbau, "Battery–less NFC sensor for pH monitoring," *IEEE Access*, vol. 7, pp. 33226–33239, 2019.
[30] A. Lazaro, M. Boada, R. Villarino, and D. Girbau, "Color measurement and analysis of fruit with a battery–less NFC sensor," *Sensors*, vol. 19, no. 7, p. 1741, Apr. 2019.
[31] D. Halperin, T. S. Heydt-Benjamin, B. Ransford, S. S. Clark, B. Defend, W. Morgan, K. Fu, T. Kohno, and W. H. Maisel, "Pacemakers and implantable cardiac defibrillators: Software radio attacks and zero–power defenses," in *Proc. IEEE Symp. Secur. Privacy (SP)*, Oakland, CA, USA, May 2008, pp. 129–142.
[32] S. Gollakota, H. Hassanieh, B. Ransford, D. Katabi, and K. Fu, "They can hear your heartbeats: Non-invasive security for implantable medical devices," *SIGCOMM Comput. Commun. Rev.*, vol. 41, no. 4, p. 2, Oct. 2011.
[33] A. J. Jara, M. A. Zamora, and A. F. G. Skarmeta, "Secure use of NFC in medical environments," in *Proc. 5th Eur. Workshop RFID Syst. Technol.*, Bremen, Germany, 2009, pp. 1–8.
[34] S. Bojjagani and V. Sastry, "A secure end-to-end proximity NFC-based mobile payment protocol," *Comput. Standards Inter.*, vol. 66, Oct. 2019, Art. no. 103348.
[35] R. Altawy and A. M. Youssef, "Security tradeoffs in Cyber physical systems: A case study survey on implantable medical devices," *IEEE Access*, vol. 4, pp. 959–979, 2016.
[36] A. Kurs, A. Karalis, R. Moffatt, J. D. Joannopoulos, P. Fisher, and M. Soljacic, "Wireless power transfer via strongly coupled magnetic resonances," *Science*, vol. 317, no. 5834, pp. 83–86, Jul. 2007.
[37] B. L. Cannon, J. F. Hoburg, D. D. Stancil, and S. C. Goldstein, "Magnetic resonant coupling as a potential means for wireless power transfer to multiple small receivers," *IEEE Trans. Power Electron.*, vol. 24, no. 7, pp. 1819–1825, Jul. 2009.
[38] M. Gebhart, J. Bruckbauer, and M. Gossar, "Chip impedance characterization for contactless proximity personal cards," in *Proc. 7th Int. Symp. Commun. Syst., Netw. Digit. Signal Process. (CSNDSP)*, Newcastle upon Tyne, TK, Jul. 2010, pp. 826–830.
[39] N. Gvozdenovic, L. W. Mayer, and C. F. Mecklenbrauker, "Measurement of harmonic distortions and impedance of HF RFID chips," in *Proc. 8th Eur. Conf. Antennas Propag. (EuCAP)*, The Hague, Netherlands, Apr. 2014, pp. 2940–2944.
[40] B. Couraud, T. Deleruyelle, E. Kussener, and R. Vauche, "Real–time impedance characterization method for RFID–type backscatter communication devices," *IEEE Trans. Instrum. Meas.*, vol. 67, no. 2, pp. 288–295, Feb. 2018.
[41] X. Qing and Z. N. Chen, "Proximity effects of metallic environments on high frequency RFID reader antenna: Study and applications," *IEEE Trans. Antennas Propagat.*, vol. 55, no. 11, pp. 3105–3111, Nov. 2007.
[42] H. Zhu, S. Lai, and H. Dai, "Solutions of metal surface effect for HF RFID systems," in *Proc. Int. Conf. Wireless Commun., Netw. Mobile Comput.*, Sep. 2007, pp. 2089–2092.
[43] H. T. Jensen and H. Lee, "Chassis NFC antenna booster," U.S. Patent 9 729 210 B2, Aug. 8, 2017.
[44] B. Lee, B. Kim, and S. Yang, "Enhanced loop structure of NFC antenna for mobile handset applications," *Int. J. Antennas Propag.*, vol. 2014, Apr. 2014, Art. no. 187029.
[45] J.-Q. Zhu, Y.-L. Ban, C.-Y.-D. Sim, and G. Wu, "NFC antenna with nonuniform meandering line and partial coverage ferrite sheet for metal cover smartphone applications," *IEEE Trans. Antennas Propagat.*, vol. 65, no. 6, pp. 2827–2835, Jun. 2017.
[46] Q. Liu, J. Zhou, and D. Chen, "NFC antenna assembly," U.S. Patent 9 941 572, Apr. 10, 2018.
[47] A. Zhao and H. Chen, "Small size NFC antenna with high performance," in *Proc. IEEE Int. Symp. Antennas Propag. (APSURSI)*, Fajardo, PR, USA, Jun. 2016, pp. 1469–1470.
[48] H. Chen and A. Zhao, "NFC antenna for portable device with metal back cover," in *Proc. IEEE Int. Symp. Antennas Propag. (APSURSI)*, Fajardo, PR, USA, Jun. 2016, pp. 1471–1472.
[49] M.-A. Chung and C.-F. Yang, "Miniaturized NFC antenna design for a tablet PC with a narrow border and metal back–cover," *IEEE Antennas Wireless Propag. Lett.*, vol. 15, pp. 1470–1474, 2016.
[50] B. Lee and F. J. Harackiewicz, "Design of a simple structured NFC loop antenna for mobile phones applications," *Prog. Electromagn. Res. C*, vol. 76, pp. 149–157, 2017.
[51] B. Jiang, J. R. Smith, M. Philipose, S. Roy, K. Sundara-Rajan, and A. V. Mamishev, "Energy scavenging for inductively coupled passive RFID systems," *IEEE Trans. Instrum. Meas.*, vol. 56, no. 1, pp. 118–125, Feb. 2007.
[52] C. Marechal and D. Paret, "The loading effect of proximity contactless smart card. incidences of impedance of the shunt regulator," in *Proc. 4th Int. Conf. Wireless Commun., Netw. Mobile Comput.*, Dalian, China, Oct. 2008, pp. 1–4.
[53] M. Gebhart, "Analytical considerations for an ISO/IEC14443 compliant SmartCard transponder," in *Proc. 11th Int. Conf. Telecommun.*, Graz, Austria, Jun. 2011, pp. 9–16.
[54] C.-H. Lu, J.-A. Li, and T.-H. Lin, "A 13.56-MHz passive NFC tag IC in 0.18-μm CMOS process for biomedical applications," in *Proc. Int. Symp. VLSI Design, Autom. Test (VLSI-DAT)*, Hsinchu, Taiwan, Apr. 2016, pp. 1–4.
[55] B. Jamali, D. C. Ranasinghe, and P. H. Cole, "Analysis of UHF RFID CMOS rectifier structures and input impedance characteristics," *Proc. SPIE*, vol. 6035, Jan. 2006, Art. no. 60350D.
[56] J. Teichmann, K. Burger, W. Hasche, J. Herrfurth, and G. Taschner, "One time programming (OTP) with Zener diodes in CMOS processes," in *Proc. Electr. Perform. Electr. Packag.*, Estoril, Portugal, Mar. 2004, pp. 433–436.
[57] Z. Zhu. (2004). *RFID Analog Front End Design Tutorial*. Auto-ID lab at University of Adelaide, pp. 3–34. Accessed: Dec. 24, 2019. [Online]. Available: https://courses.e-ce.uth.gr/ECE438/tutorials/RFIDanadesign.pdf
[58] J. Hu, S. Wu, K. Lin, and H. Tan, "Low-power energy supply circuit for passive RFID transponder," in *Proc. IEEE Int. Conf. RFID*, Orlando, FL, USA, Apr. 2009, pp. 1–6.

[59] F. Alcalde, O. Alpago, and J. Lipovetsky, "CMOS design of an RFID interface compatible with ISO/IEC–14443 type a protocol," in *Proc. Argentine Conf. Micro-Nanoelectron., Technol. Appl. (EAMTA)*, Mendoza, Argentina, Jul. 2014, pp. 41–47.

[60] J. Hu, H. Tan, and Y. Xu, "A novel design of low power RFID tag interface circuit," in *Proc. IET Conf. Wireless, Mobile Sensor Netw. (CCWMSN)*, Shanghai, China, Dec. 2007, pp. 478–481.

[61] *Mosis Integrated Circuit Fabrication Service*. Accessed: Dec. 24, 2019. [Online]. Available: https://www.mosis.com/vendors/view/tsmc/018

[62] C. Y. Tan, B. Statham, R. Marks, and P. A. Payne, "Skin thickness measurement by pulsed ultrasound; its reproducibility, validation and variability," *Brit. J. Dermatology*, vol. 106, no. 6, pp. 657–667, 1982.

[63] S. Huclova, D. Erni, and J. Fröhlich, "Modelling and validation of dielectric properties of human skin in the MHz region focusing on skin layer morphology and material composition," *J. Phys. D, Appl. Phys.*, vol. 45, no. 2, Jan. 2012, Art. no. 025301.

[64] C. Gabriel, S. Gabriel, and E. Corthout, "The dielectric properties of biological tissues: I. Literature survey," *Phys. Med. Biol.*, vol. 41, no. 11, pp. 2231–2249, Nov. 1996.

[65] S. Gabriel, R. W. Lau, and C. Gabriel, "The dielectric properties of biological tissues: II. Measurements in the frequency range 10 Hz to 20 GHz," *Phys. Med. Biol.*, vol. 41, no. 11, pp. 2251–2269, Nov. 1996.

[66] S. Gabriel, R. W. Lau, and C. Gabriel, "The dielectric properties of biological tissues: III. Parametric models for the dielectric spectrum of tissues," *Phys. Med. Biol.*, vol. 41, no. 11, pp. 2271–2293, Nov. 1996.

[67] F. W. Grover, *Inductance Calculations: Working Formulas and Tables*, Mineola, NY, USA: Dover, Jan. 2009.

[68] L. Youbok, "Antenna circuit design for RFID applications," Microchip Technol., Chandler, AZ, USA, Appl. Note AN710, 2003. [Online]. Available: http://ww1.microchip.com/downloads/en/appnotes/00710c.pdf

[69] P. E. K. Donaldson and E. Sayer, "A technology for implantable hermetic packages—Part 2: An implementation," *Med. Biol. Eng. Comput.*, vol. 19, no. 4, pp. 403–405, Jul. 1981.

[70] H. Wheeler, "Formulas for the skin effect," *Proc. IRE*, vol. 30, no. 9, pp. 412–424, Sep. 1942.

[71] C. Dichtl, P. Sippel, and S. Krohns, "Dielectric properties of 3D printed polylactic acid," *Adv. Mater. Sci. Eng.*, vol. 2017, Jun. 2017, Art. no. 6913835.

[72] K. Fotopoulou and B. W. Flynn, "Wireless power transfer in loosely coupled links: Coil misalignment model," *IEEE Trans. Magn.*, vol. 47, no. 2, pp. 416–430, Feb. 2011.

[73] M. Ishii and K. Komiyama, "A measurement method for the antenna factor of small loop antenna by measuring the input impedance," in *Proc. Conf. Precis. Electromagn. Meas.*, London, U.K., Jun. 2004, pp. 80–81.

[74] K. Na, H. Jang, H. Ma, and F. Bien, "Tracking optimal efficiency of magnetic resonance wireless power transfer system for biomedical capsule endoscopy," *IEEE Trans. Microw. Theory Techn.*, vol. 63, no. 1, pp. 295–304, Jan. 2015.

[75] M. Kiani and M. Ghovanloo, "An RFID–based closed–loop wireless power transmission system for biomedical applications," *IEEE Trans. Circuits Syst. II, Exp. Briefs*, vol. 57, no. 4, pp. 260–264, Apr. 2010.

[76] Y.-P. Lin, C.-Y. Yeh, P.-Y. Huang, Z.-Y. Wang, H.-H. Cheng, Y.-T. Li, C.-F. Chuang, P.-C. Huang, K.-T. Tang, H.-P. Ma, Y.-C. Chang, S.-R. Yeh, and H. Chen, "A battery–less, implantable Neuro–electronic interface for studying the mechanisms of deep brain stimulation in rat models," *IEEE Trans. Biomed. Circuits Syst.*, vol. 10, no. 1, pp. 98–112, Feb. 2016.

[77] D. Jiang, D. Cirmirakis, M. Schormans, T. A. Perkins, N. Donaldson, and A. Demosthenous, "An integrated passive phase–shift keying modulator for biomedical implants with power telemetry over a single inductive link," *IEEE Trans. Biomed. Circuits Syst.*, vol. 11, no. 1, pp. 64–77, Feb. 2017.

[78] M. Kiani and M. Ghovanloo, "A 13.56-Mbps pulse delay modulation based transceiver for simultaneous near–field data and power transmission," *IEEE Trans. Biomed. Circuits Syst.*, vol. 9, no. 1, pp. 1–11, Feb. 2015.

[79] H. Saghlatoon, R. Mirzavand, M. M. Honari, and P. Mousavi, "Investigation on passive booster for improving magnetic coupling of metal mounted proximity range HF RFIDs," *IEEE Trans. Microw. Theory Techn.*, vol. 65, no. 9, pp. 3401–3408, Sep. 2017.

ANTONIO LAZARO (Senior Member, IEEE) was born in Lleida, Spain, in 1971. He received the M.S. and Ph.D. degrees in telecommunication engineering from the Universitat Politècnica de Catalunya (UPC), Barcelona, Spain, in 1994 and 1998, respectively. He then joined the faculty of UPC, where he currently teaches a course on microwave circuits and antennas. Since July 2004, he has been a full-time Professor with the Department of Electronic Engineering, Universitat Rovira i Virgili (URV), Tarragona, Spain. His research interests are microwave device modeling, on-wafer noise measurements, monolithic microwave integrated circuits (MMICs), low phase noise oscillators, MEMS, RFID, UWB, and microwave systems.

MARTÍ BOADA received the B.S. degree in telecommunications engineering from Universitat Rovira i Virgili (URV), Tarragona, Spain, in 2012, and the M.S. degree in telecommunications engineering and management from the Universitat Politècnica de Catalunya (UPC), Barcelona, Spain, in 2014. He is currently pursuing the Ph.D. degree with the Department of Electronic Engineering, URV. His research activity focuses on microwave devices and systems, with an emphasis on RFID, NFC, and wireless sensors.

RAMON VILLARINO received the Telecommunications and Technical Engineering degree from Ramon Llull University (URL), Barcelona, Spain, in 1994, and the Senior Telecommunications Engineering and Ph.D. degrees from the Polytechnic University of Catalonia (UPC), Barcelona, in 2000 and 2004, respectively. From 2005 to 2006, he was a Research Associate with the Technological Telecommunications Center of Catalonia (CTTC), Barcelona. He was with the Autonomous University of Catalonia (UAB) as a Researcher and an Assistant Professor, from 2006 to 2008. Since January 2009, he has been a full-time Professor with Universitat Rovira i Virgili (URV). His research activities are oriented toward radiometry, microwave devices and systems based on UWB, RFIDs, and frequency selective structures using metamaterials (MMs).

DAVID GIRBAU (Senior Member, IEEE) received the B.S. degree in telecommunication engineering, the M.S. degree in electronics engineering, and the Ph.D. degree in telecommunication from the Universitat Politècnica de Catalunya (UPC), Barcelona, Spain, in 1998, 2002, and 2006, respectively. From February 2001 to September 2007, he was a Research Assistant with UPC. From September 2005 to September 2007, he was also a part-time Assistant Professor with the Universitat Autònoma de Barcelona (UAB). Since October 2007, he has been a full-time Professor with Universitat Rovira i Virgili (URV). His research interest includes microwave devices and systems, with an emphasis on UWB, RFIDs, RF-MEMS, and wireless sensors.